nature portfolio

https://doi.org/10.1038/s41586-022-05061-w

Supplementary information

A dynamically reprogrammable surface with self-evolving shape morphing

In the format provided by the authors and unedited

Supporting Information

A dynamically reprogrammable metasurface with self-evolving shape morphing

Yun Bai[1,14], Heling Wang[2,3,4,5,6,14], Yeguang Xue[2,3,4], Yuxin Pan[1], Jin-Tae Kim[7], Xinchen Ni[7], Tzu-Li Liu[7], Yiyuan Yang[3], Mengdi Han[7,8], Yonggang Huang[2,3,4,7,*], John A. Rogers[2,3,4,7,9,10,11,12,*], and Xiaoyue Ni[1,7,13,*]

[1]Department of Mechanical Engineering and Materials Science, Duke University, Durham, NC, USA
[2]Department of Civil and Environmental Engineering, Northwestern University, Evanston, IL, USA
[3]Department of Mechanical Engineering, Northwestern University, Evanston, IL, USA
[4]Department of Materials Science and Engineering, Northwestern University, Evanston, IL, USA
[5]Laboratory of Flexible Electronics Technology, Tsinghua University, Beijing, China
[6]Institute of Flexible Electronics Technology of THU Jiaxing, Zhejiang, China
[7]Querrey Institute for Bioelectronics, Northwestern University, Evanston, IL, USA
[8]Department of Biomedical Engineering, College of Future Technology, Peking University, Beijing, China
[9]Department of Biomedical Engineering, Northwestern University, Evanston, IL, USA
[10]Department of Neurological Surgery, Feinberg School of Medicine, Northwestern University, Chicago, IL, USA
[11]Department of Chemistry, Northwestern University, Evanston, IL, USA
[12]Department of Electrical and Computer Engineering, Northwestern University, Evanston, IL, USA
[13]Department of Biostatistics and Bioinformatics, Duke University, Durham, NC, USA
[14]These authors contribute equally

Corresponding Author:

helingwang1@gmail.com (H.W.); y-huang@northwestern.edu (Y.H.); jrogers@northwestern.edu (J.A.R.); xiaoyue.ni@duke.edu (X.N.)

This Supplementary Information includes:

Further Supplementary Materials:

Supplementary Videos 1 to 7 (.mp4)

Table of Contents

Supplementary Note S1: Fabrication procedures for the metasurface

Sacrificial layer

1. Clean silicon wafers with acetone and methanol.

2. Spin coat PMMA to produce a sacrificial layer (3000 rpm, 30 s; bake at 180 °C, 30 s)

Bottom PI layer

3. Spin coat PI2545 (1500 rpm, 30 s; bake at 110 °C, 180 s; bake at 150 °C, 180 s; vacuum bake at 260 °C, 45 min; fully cure)

Metal layer

4. Deposit Ti/Au (10 nm/300 nm in thickness) using electron-beam evaporation.

5. Define metal pattern using photoresist (S1813, 3000 rpm) and wet etching (Au/Ti etchant).

Top PI layer

6. Spin coat PI2545 (1500 rpm, 30s; bake at 110 °C, 180 s; bake at 150°C, 180 s; vacuum bake at 260 °C, 45 min)

7. Deposit Cu (50 nm) using electron beam evaporation.

8. Define Cu pattern as hard mask using photoresist (S1813, 3000 rpm) and wet etching (Cu etchant).

9. Dry etch of PI in reactive ion etcher (RIE) with CF_3 and CF_4.

10. Remove the Cu hard mask using wet etching (Cu etchant).

Transfer printing

11. Undercut PMMA sacrificial layer in acetone.

12. Transfer sample from silicon wafer to water soluble tape.

13. Dissolve water soluble tape with warm water to make sample freestanding.

Supplementary Note S2: Finite element analysis (FEA)

S2.1 Deformation actuated by the Lorentz force

FEA was performed to simulate the deformation of the serpentine-shaped mesh structures actuated by Lorentz force. A home-made python script was combined with the commercial software ABAQUS to model the coupling of electrical current, magnetic field and structural deformation, which was not directly available in ABAQUS[S1]. The detailed process was reported in the supplementary note of a previous paper of our group[S2]. In brief, given the port voltages as boundary conditions, the distribution of electric current density was simulated by ABAQUS, transferred to the python script to calculate the distribution of the Lorentz force per unit volume, and then the force was transferred back to ABAQUS to simulate the deformation. The simulation was divided into several loading steps (typically K = 10~20), with a small portion (1/K) of the total voltages added in each step. Refined mesh with feature size smaller than 1/10 of the ribbon width (b_{PI}) ensured the accuracy. The elastic modulus (E) and Poisson's ratio (v) were E_{PI} = 2.5 GPa and v_{PI} = 0.34, respectively for PI, and E_{Au} = 78 GPa and v_{Au} = 0.42, respectively for Au. The electrical resistivity of Au was $\rho_{Au} = 2.43\times10^{-8}$ m·Ω.

The non-uniform magnetic field generated by the cuboidal magnet (length $2a_{mag}$, magnetization M along z'- direction in the local $x'y'z'$ coordinate system, see Supplementary Fig.29a) was calculated by the formula below[S3]

$$
\begin{aligned}
B_{x'} &= \frac{\mu_0 M}{4\pi}\ln\left[\frac{F_2(-x',y',-z')F_2(x',y',z')}{F_2(x',y',-z')F_2(-x',y',z')}\right] \\
B_{y'} &= \frac{\mu_0 M}{4\pi}\ln\left[\frac{F_2(-y',x',-z')F_2(y',x',z')}{F_2(y',x',-z')F_2(-y',x',z')}\right] \\
B_{z'} &= -\frac{\mu_0 M}{4\pi}\ln\left[\begin{array}{l}F_1(-x',y',z')+F_1(-x',y',-z')+F_1(-x',-y',z')+F_1(-x',-y',-z')+\\ F_1(x',y',z')+F_1(x',y',-z')+F_1(x',-y',z')+F_1(x',-y',-z')\end{array}\right]
\end{aligned}
\quad , \quad \text{(S1)}
$$

with

$$F_1(x',y',z') = \arctan\left[\frac{(x'+a_{\mathrm{mag}})(y'+a_{\mathrm{mag}})}{(z'+a_{\mathrm{mag}})\sqrt{(x'+a_{\mathrm{mag}})^2+(y'+a_{\mathrm{mag}})^2+(z'+a_{\mathrm{mag}})^2}}\right]$$

$$F_2(x',y',z') = \arctan\left[\frac{\sqrt{(x'+a_{\mathrm{mag}})^2+(y'-a_{\mathrm{mag}})^2+(z'+a_{\mathrm{mag}})^2}+a_{\mathrm{mag}}-y'}{\sqrt{(x'+a_{\mathrm{mag}})^2+(y'+a_{\mathrm{mag}})^2+(z'+a_{\mathrm{mag}})^2}-a_{\mathrm{mag}}-y'}\right], \quad \text{(S2)}$$

and where μ_0 is the magnetic permeability of free space. The magnetization was M = 1.1×10^6 A/m such that the magnetic field at the surface (x' = y' = 0, z' = a_{mag}) was ~400 mT.

S2.2 Temperature change due to Joule heating

The temperature change due to Joule heating of a single serpentine was simulated by the structure-electricity-heat coupling module of ABAQUS. The geometry was imported from the deformed shape simulated by the process in Supplementary Note S2.1. The Joule heat per unit volume was calculated by ABAQUS according to the simulated electric current density. Convective heat transfer with air was applied to all external surfaces of the structure. Steady-state heat transfer analysis then gave the balanced temperature distribution. The baseline values of parameters were I = 10 mA, ρ_{Au} = 2.43×10^{-8} m·Ω, b_{PI} = 100 μm, $b_{\mathrm{Au}}/b_{\mathrm{PI}}$ = 0.95, a= 0.3 μm, and the convective heat transfer coefficient with air H_{Air} = 50 W/(m^2·K).

Supplementary Note S3: Analytical model and scaling law for the deformation

S3.1 Analytical model of a single serpentine structure

Supplementary Fig. 2a shows the 2D precursor of a single serpentine structure of total length L , with two fixed ends. It consists of N semi-circular rings, connected by N-1 straight ribbons with length H. The distance between the two adjacent straight ribbons is $\lambda = L/N$ (measured from the central axis, $\lambda \ll L$, H). The semi-circular rings at the two ends of the serpentine structure are also connected by straight ribbons (length $H/2$) to the bonding sites. The nth semi-circular ring is located at $Y = Y_n = -L/2 + (n-1)\lambda$. The cross-sectional

width (b_{PI}) and thickness (h_{PI}) of the semi-circular rings and straight ribbons are uniform, with the Au thickness being much smaller than PI thickness.

The serpentine structure deforms into 3D when it is placed in uniform magnetic field *B* (along negative *X*-direction in Supplementary Fig. 2a) and actuated by electric current I. For the level of deformation studied in this manuscript (*i.e.*, maximum out-of-plane displacement u/L on the order of 10%), the following simplifications can be made. The semi-circular ring undergoes only out-of-plane (*Z*-direction) rigid-body displacement $u^Z\left(Y^n\right)$ with no rotation such that it remains horizontal. The straight ribbon undergoes out-of-plane displacement (denoted by Δ_n for the straight ribbon that connects the semi-circular ring *n* to *n*–1) and bending. The boundary conditions are $\Delta_n\left[\left(-1\right)^{n-1}\frac{L}{2}\right]=u_Z\left(Y_n\right)$, $\Delta_n\left[\left(-1\right)^{n}\frac{L}{2}\right]=u_Z\left(Y_{n-1}\right)$ and $\frac{\mathrm{d}\Delta_n}{\mathrm{d}X}\left(\pm\frac{L}{2}\right)=0$, and following force balance the internal force in *Z*- direction is $P_n=-BIY_n$. Based on beam theory,

$$u_Z\left(Y_n\right)-u_Z\left(Y_{n-1}\right)=\frac{P_nH^3}{E_{\mathrm{PI}}b_{\mathrm{PI}}h_{\mathrm{PI}}^3}=-\frac{BIH^3}{E_{\mathrm{PI}}b_{\mathrm{PI}}h_{\mathrm{PI}}^3}Y_n, \tag{S3}$$

where $E_{\mathrm{PI}}b_{\mathrm{PI}}h_{\mathrm{PI}}^3$ is the bending rigidity with the contribution of Au layer neglected, as Au thickness (0.3 μm) is much smaller than PI thickness (~10 μm). Considering that $\lambda<<L$ and the serpentine structure is fixed at two ends, the maximum out-of-plane displacement is

$$u=u_Z\left(Y=0\right)=-\frac{BIH^3}{E_{\mathrm{PI}}b_{\mathrm{PI}}h_{\mathrm{PI}}^3}\sum_{n=1}^{N/2}Y_n\approx-\frac{BIH^3}{E_{\mathrm{PI}}b_{\mathrm{PI}}h_{\mathrm{PI}}^3\lambda}\int_{-L/2}^{0}Y\mathrm{d}Y=\frac{BIH^3L^2}{8E_{\mathrm{PI}}b_{\mathrm{PI}}h_{\mathrm{PI}}^3\lambda}. \tag{S4}$$

In Eq. (S4), *BIL* is the effective Lorentz force and $\frac{E_{\mathrm{PI}}b_{\mathrm{PI}}h_{\mathrm{PI}}^3\lambda}{H^3L}$ may be defined as the effective rigidity of the serpentine structure, such that the displacement is proportional to the effective force divided by the effective rigidity. This analytical solution (Eq. (S4)) matches well with FEA (see Supplementary Note S2 for details), as shown in Supplementary Fig. 2b. In the FEA validation, the dots are for FEA with the baseline values of parameters being B = 150 mT, I = 10 mA, H = 2 mm, L = 5 mm, E_{PI} = 2.5 GPa, b_{PI} = 100 μm, h_{PI} = 7.8 μm and λ = 200 μm, and each of these 8 parameters varies independently in its representative range; the straight line corresponds to the analytical solution (Eq. (S4)) with slope being 0.125. As suggested by Eq. (S4),

increasing the total serpentine width H or decreasing the PI thickness h_{PI} increases the deformation ($u \propto H^3$, $1/h_{\mathrm{PI}}^3$), thereby providing a design guideline for a tunable electromagnetic response in a broad range of magnetic field strengths. For example, increasing H by 33% and decreasing h_{PI} by 33% enables the serpentine structure to exhibit approximately the same deformation for magnetic field strengths reduced by one order of magnitude, as shown in Extended Data Fig. 2.

For modest current such that the temperature change due to Joule heating is small and therefore the change in the electrical resistivity (ρ_{Au}) can be neglected, the current *I* is linearly proportional to the applied voltage *V* via $I \approx \frac{V \lambda b_{\mathrm{Au}} h_{\mathrm{Au}}}{\rho_{\mathrm{Au}} HL}$ (noticing that $\lambda << H, L$). Therefore, the out-of-plane displacement is related to the voltage via

$$u = \frac{BVH^2 L b_{\mathrm{Au}} h_{\mathrm{Au}}}{8 E_{\mathrm{PI}} b_{\mathrm{PI}} h_{\mathrm{PI}}^3 \rho_{\mathrm{Au}}}. \qquad \text{(S5)}$$

S3.2 Scaling law for the deformation of the array of *N* serpentine beams structure

Supplementary Fig. 8 shows an array of *N* serpentine beams (along *Y*-direction, labeled as S_{Y1}, S_{Y2},…, S_{YN}, S_{YN+1},…, S_{Y2N}) connected by *N*+1 serpentines along *X*-direction (labeled as S_{X0}, S_{X1},…, S_{XN}). There is no metal layer in serpentine S_{Xi} (*i* = 0,1,…,*N*) such that the electric currents in serpentine S_{Yj} and S_{YN+j} are the same (denoted as I_j), and each of I_j can be applied independently via port voltages. Applying voltage V_j to induce electric current I_j in only two serpentines (S_{Yj} and S_{YN+j}), dimensional analysis suggests that the effective Lorentz force is BI_jL and the effective rigidity of the serpentine structure is proportional to $\frac{E_{\mathrm{PI}} b_{\mathrm{PI}} h_{\mathrm{PI}}^3 \lambda}{H^3 L}$, such that the displacement of node *j* (intersection of serpentine S_{Yj} and S_{YN+j}), proportional to the effective force divided by the effective rigidity, follows the same scaling as in Eq. (S4) and Eq. (S5), with a revised slope to account for the mechanical coupling among the serpentines, *i.e.*, $u_n \propto \frac{BI_j H^3 L^2}{E_{\mathrm{PI}} b_{\mathrm{PI}} h_{\mathrm{PI}}^3 \lambda}$ and $u_n \propto \frac{BH^2 L b_{\mathrm{Au}} h_{\mathrm{Au}}}{E_{\mathrm{PI}} b_{\mathrm{PI}} h_{\mathrm{PI}}^3 \rho_{\mathrm{Au}}} V_j$. When all the port voltages V_j are applied simultaneously, under the linear assumption

such that the principle of linear superposition applies, the displacements u_n are still linearly dependent on port voltages V_j and the coefficients in the linear relationship scale with $\frac{BH^2Lb_{\mathrm{Au}}h_{\mathrm{Au}}}{E_{\mathrm{PI}}b_{\mathrm{PI}}h_{\mathrm{PI}}^3\rho_{\mathrm{Au}}}$.

S3.3 Scaling law for the deformation of the *N*×*N* structures

Supplementary Fig. 9 shows a serpentine-shaped mesh structure consisting of $N \times (N+1)$ serpentines along *X*- direction (labeled as S_1, S_2,…, $S_{N(N+1)}$, length L_{S}) connected by $(N+1) \times N$ serpentines along *Y*-direction (labeled as $S_{N(N+1)+1}$, $S_{N(N+1)+2}$,…, $S_{2N(N+1)}$, length L_{S}). The geometries of all the serpentines are the same. Port voltages V_j (j = 1,2,…,4N) are applied at the peripheries of the structure to induce electric currents I_i (i = 1,2,…,2N(N+1)) in the serpentines. The resistance of each serpentine is $R \approx \frac{\rho_{\mathrm{Au}}L_{\mathrm{S}}H}{\lambda b_{\mathrm{Au}}h_{\mathrm{Au}}}$ (noticing that λ<<H, L_{S}). Given N, L_{S} is linearly proportional to the overall size L of the structure, such that $R \propto \frac{\rho_{\mathrm{Au}}LH}{\lambda b_{\mathrm{Au}}h_{\mathrm{Au}}}$. Therefore, dimensional analysis suggests that the electric currents are linearly dependent on the port voltages via

$$I_i = \frac{\lambda b_{\mathrm{Au}}h_{\mathrm{Au}}}{\rho_{\mathrm{Au}}HL}\sum_{j=1}^{4N}\tilde{D}_{ij}V_j\,, \qquad \text{(S6)}$$

with the dimensionless coefficients $\tilde{D}_{ij}$ depending on the geometry. Dimensional analysis also suggests that the displacements induced by current I_i follows the same scaling as in Eq. (S4) with a revised slope to account for the mechanical coupling among the serpentines, *i.e.*, $u_n \propto \frac{BH^3L_{\mathrm{S}}^2}{E_{\mathrm{PI}}b_{\mathrm{PI}}h_{\mathrm{PI}}^3\lambda}I_i \propto \frac{BH^3L^2}{E_{\mathrm{PI}}b_{\mathrm{PI}}h_{\mathrm{PI}}^3\lambda}I_i$ (given N). Therefore, under the linear assumption, the principle of linear superposition in combination with Eq. (S6), suggests that the displacements u_n are linearly dependent on the port voltages V_j and the coefficients in the linear relationship scale with $\frac{BH^2Lb_{\mathrm{Au}}h_{\mathrm{Au}}}{E_{\mathrm{PI}}b_{\mathrm{PI}}h_{\mathrm{PI}}^3\rho_{\mathrm{Au}}}$.

Supplementary Note S4: Theoretical model of the temperature change due to Joule heating

For a segment of Au (length δL) encapsulated in PI (temperature T; see Supplementary Fig. 2a for the

cross-sectional view), the heat generated by Joule heating per unit time (power) is $W_{\text{Generate}} = \frac{I^2 \rho_{\text{Au}} \delta L}{b_{\text{Au}} h_{\text{Au}}}$. The convective heat transfer per unit time with air (H_{Air}—convective heat transfer coefficient, T_{Air}—air temperature) is $W_{\text{Loss}} = 2b_{\text{PI}}(\delta L) H_{\text{Air}}(T - T_{\text{Air}})$. Energy balance $W_{\text{Generate}} = W_{\text{Loss}}$ leads to

$$\Delta T = T - T_{\text{Air}} = \frac{I^2 \rho_{\text{Au}}}{2b_{\text{PI}} b_{\text{Au}} h_{\text{Au}} H_{\text{Air}}}. \quad \text{(S7)}$$

As before applying the electric current, temperature of the structure is the same as the air temperature, ΔT is also the temperature change due to Joule heating. This analytical solution (Eq. (S7)) is quite accurate to predict the temperature change of a single serpentine structure, as shown in Supplementary Fig. 2c. In the FEA validation, the dots are for FEA of the maximum temperature change in the serpentine, with the baseline values of parameters being I = 10 mA, ρ_{Au} = 2.43×10^{-8} m·Ω, b_{PI} = 100 μm, $b_{\text{Au}}/b_{\text{PI}}$ = 0.95, h_{Au} = 0.3 μm, and H_{Air} = 50 W/(m^2·K), and each of these 6 parameters varies independently in its representative range; the straight line corresponds to the analytical solution (Eq. (S7)) with slope being 0.5.

For the temperature change ΔT to be smaller than a threshold ΔT_{Upper} (*i.e.,* the upper limit of the temperature that the material can tolerate or allowed in biomedical application), the upper limit of the electric current is

$$I \le I_{\text{Upper}} = \sqrt{\frac{2b_{\text{PI}} b_{\text{Au}} h_{\text{Au}} H_{\text{Air}} \Delta T_{\text{Upper}}}{\rho_{\text{Au}}}}. \quad \text{(S8)}$$

Eq. (S8), combined with Eq. (S4), gives the upper limit of the deformation of the single serpentine structure as

$$u_{\text{Upper}} \le \frac{BH^3 L^2}{8E_{\text{PI}} h_{\text{PI}}^3 \lambda} \sqrt{\frac{2b_{\text{Au}} h_{\text{Au}} H_{\text{Air}} \Delta T_{\text{Upper}}}{b_{\text{PI}} \rho_{\text{Au}}}}. \quad \text{(S9)}$$

Supplementary Note S5: Experimental characterizations of a single serpentine beam

S5.1 Mechanical behaviors under electromagnetic actuation

Supplementary Fig. 3a shows a schematic illustration of the experimental configuration. The static magnetic field is generated by two parallel disks of Neodymium magnets spaced apart, each with a surface magnetic field of ~264 mT. A customized 3D printed magnet mounting stage can adjust the spacing between the magnets. The magnetic setup presented in the main text takes a default 55-mm spacing. Supplementary Fig. 3b shows the magnetic flux density measured by a gaussmeter (GMHT201, Apex Magnets) across the center (*O*) along *X*-axis and *Y*-axis in the setup. The field strength in the *X*-direction, B_X, is 224 ± 16 mT, around the center (*O*). A movable and rotatable sample stage has a fixed height that levels with the center of the magnets. The model-driven process takes the average field strength around the center and ignores any spatial variance.

Extended Data Fig. 1c shows that a serpentine beam carrying a current density **J** (along *Y*-axis) deforms locally under the electromagnetic force, $\mathbf{F}_{EM} = \mathbf{J} \times \mathbf{B}$. The serpentine beam ($\lambda << H$) exhibits a linear, spring-like behavior when deformed out of the sample plane under the electromagnetic actuation (Supplementary Note S2.1). A side camera (Webcams, ELP, 3840×2160-pixel resolution, 30 fps) monitors the out-of-plane deformation (u) and any irreversible deformation (u') of the beam (Extended Data Fig. 1d). An imaging process via ImageJ 1.x pipeline produces displacement measurements with a resolution of 0.006 mm and an uncertainty of ±0.055 mm (Supplementary Fig. S30). The measured displacement u increases linearly with the actuation current I in the elastic regime, within which the electro-magneto-mechanical behavior of the beam agrees with both analytical solution and finite element analysis study (Extended Data Fig. 1e). When the actuation current exceeds 27.5 mA, the measured u deviates from the elastic behavior, and a sub-mm irreversible deformation (u') is observed subsequently when unloaded (Extended Data Fig. 1f). Based on the experimental observations, the single-beam sample can deform to a maximum of 4.2 ± 0.1 mm ($u/L \approx 38\%$) while remaining fully reversible, under a maximum current of 27.5 mA ($J < 7 \times 10^8$ A/m^2; the cross-section area of Au is 3.9×10^{-11} m^2).

Extended Data Fig. 2a shows serpentine beam structures of the same length (L = 11.0 mm) but different widths (H = 0.84 mm, 1.20 mm, 1.56 mm). In a magnetic field of 224 mT, the current-controlled mechanical responses of the beams with various thicknesses (h_{PI} = 5.0 μm, 7.5 μm, and 12.0 μm) agree with the analytical predictions (Eq. (S4)). The metasurface presented in the main text adopts the serpentine-beam design with H = 1.20 mm and h_{PI}= 7.5 μm and deforms in a magnetic field of 224 mT. Following the scaling law (Eq. (S4), Extended Data Fig. 1b), a beam with H increased by a factor of g_H, bdecreased by a factor g_h can maintain the same Lorentz-driven mechanical response in a magnetic field with strength reduced to a factor of $(1 + g_H)^{-3}(1 - g_h)^3$. Extended Data Fig. 2c shows that a beam with H = 1.56 mm (increased by 30%) and h_{PI} = 5.0 μm (decreased by 33%) performs approximately the same level of deformation (u ~2.25 mm) under the same current (I = 15 mA) in a smaller magnetic field of 25 mT (reduced by ~90% by spacing the magnets apart from 55 mm to 175 mm). The reduced field strength is comparable to that generated by a commercial Helmholtz coil (SpinCoil-7-X, customized, Micro Magnetics, Inc.; coil radius R_c = 18 mm, number of turns n = 2500, coil current I = 2 A) over a large distance (~160 mm). Based on the physics of the response, by reducing the PI thickness or replacing it with a low-modulus encapsulation material such that its contribution to the bending rigidity is negligible, the magnetic field may be reduced to an extreme of ~0.2 mT for the redesigned structure to maintain the same Lorentz-driven response, given the limit on the electric current and overall structure size.

S5.2 Thermal behaviors under electromagnetic actuation

Thermal imaging of a single-beam sample heated by a temperature-controlled hot plate calibrates the infrared camera (FLIR E60) in the temperature range (20–80 °C). The calibrated camera measures the equilibrium temperature of the sample under a current ranging from 0 to 40 mA (at room temperature of 25 °C). Extended Data Fig. 1g shows the measured temperature versus applied current, which is consistent

with the analytical prediction validated by FEA (Supplementary Note S4). The temperature change (ΔT) induced by Joule heating under a current of 27 mA is ~35 °C upon equilibrium (at room temperature of 25 °C).

S5.3 Response time under electromagnetic actuation

The single-beam sample is actuated by an applied current I (I = 10 mA, u/L ~14%). The dynamic response of the single beam is monitored by a side camera (Canon EOS R, 60 fps). Supplementary Fig. 5 shows that the sample goes through vibrations before reaching a steady state where no displacement deviation can be identified in sequential frames in the recorded video. The experimental observation shows that the single-beam sample reaches a steady state within 0.07 s (Supplementary Fig. 5).

S5.4 Cycling test under electromagnetic actuation

The single-beam sample undergoes a current-controlled high-cycle test. The sample deforms bi-directionally over 1000 cycles at a frequency of 1 Hz with a displacement amplitude u monitored by a side camera for both small deformation (u/L ~14%, I = 10 mA) and large deformation (u/L ~28%, I = 20 mA). Supplementary Fig. 6a, b shows that the single-beam sample under the current cycles of ±10 mA exhibits a fully-reversible deformation behavior over 1,000 cycles with a constant displacement amplitude, u = 1.55 ± 0.02 mm (u/L ~14%). Supplementary Fig. 6c, d shows the results of the cycling test under the current amplitude of ±20 mA. The single-beam sample maintains a fully-reversible deformation behavior over the first 500 cycles with a constant displacement amplitude, u = 3.08 ± 0.06 mm (u/L ~28%). Upon the remaining 500 cycles, both the mean value and the standard deviation of the displacement amplitude increase with the cycles, yielding an average amplitude, u = 3.18 ± 0.18 mm (u/L ~29%), for the last 100 cycles. Overall, the single-beam sample deforms with an amplitude, u = 3.10 ± 0.12 mm (u/L ~28%) under the cycling current of ±20 mA over 1,000 cycles at the frequency of 1 Hz.

Supplementary Note S6: Optimization algorithm of the experiment-driven process

S6.1 Loss function and optimization

In the experiment-driven process, the real-time imaging evaluates the difference between the current shape (u_i) and the target shape (u^*), providing an in-situ nodal displacement error analysis. Changes in the actuation, $\mathbf{V} = \{V_j\}$, will update the loss function, $f(\mathbf{V}) = \sum_i e_i^2$, defined as the sum of squared error (normalized by system size as $e_i = (u_i - u_i^*)/L$). Sequential Least Squares Programming (SLSQP), a gradient-descent based algorithm, computes the Jacobian matrix to minimize the loss function. For each update on V_j (the voltage input at the jth port), a 3-point method requires two function evaluations to calculate the numerical approximation of the Jacobian matrix. Each iteration requires $4\times(N+M)$ function evaluations for the Jacobian calculation and an additional 2 function evaluations for the step-size calculation to check on the constraints.

Extended Data Fig. 4a–c shows three representative optimization processes for a 4×4 sample to morph into Shape I, III, IV (see Extended Data Fig. 5 and Supplementary Note S8), with the loss function $f(\mathbf{V})$ monitored over 15 iterations. According to the experimental observation, $f(\mathbf{V})$ (with an initial value, $f(\mathbf{V} = \mathbf{0})$, in the range of 0.05–0.35) drops by ~99.5% and reaches a steady state in 5–15 iterations. A maximum final loss, $0 \le 0.005 f(\mathbf{V} = \mathbf{0})$, and a maximum of 15 iterations set the stopping criteria for the optimization process.

S6.2 Limitations in experiment-driven optimization

For the 4×4 and 8×8 morphing structures presented in the manuscript, the optimization problems are theoretically convex as the objective functions (displacement vs. voltage) and constraints (current vs. voltage) are all approximately linear. In the experiment, discreteness in digitization and measurement uncertainties add complexity to the error surface. Experimental noise and constraints impose limitations on the performance of the gradient-based optimization process. The major limiting factors in the current setup are

the discrete actuation voltages, the maximum actuation allowed for reversible deformation, and the 3D imaging noise (δu = 0.016 mm, Supplementary Note S14). The discrete actuation comes from the 12-bit pulse-width modulation (PWM) drivers followed by the voltage amplifier circuits, which provide actuation voltages in the range of 0–6 V in a discrete step of ~0.0015 V. The mechanical and thermal characterizations (Supplementary Note S5) suggest the maximum allowed current for reversible deformation to be 27 mA. FEA simulation provides a linear relation between the current flow (**I**) in each serpentine beam and the portal voltages (**V**) as $\mathbf{I} = \mathbf{C}^{\mathrm{I}}\mathbf{V}$. This model prediction of I based on applied **V** serves as a virtual current monitor to set voltage constraints to ensure that the current is below the maximum allowed value (27 mA) everywhere in the sample.

Extended Data Fig. 6a shows a simulation result of the impact of the experimental noise and constraints on the optimization. The simulation takes the linear model (Eq. 1) with noises and constraints characterized from the experiment and evaluates the final loss f_0 of a 4×4 sample morphing target shape (Fig. 3b) post 15 iterations. The distribution of f_0 from the simulation (1,000 trials) agrees with that from the experiment (97 trials) given 3D imaging noise δu = 0.016 mm,12-bit PWM output, and a maximum current I_{max} = 27 mA. Extended Data Fig. 6b shows the impact of the discrete voltage on the optimization process without imaging noise. The final loss can reach 4.96×10^{-5} in the case of 12-bit PWM signal. A 20-bit resolution gives a final loss of 3.30×10^{-5} that is comparable to that resulted from continuous, analog signal. Extended Data Fig. 6c–f shows the distribution of f_0 from the simulation (1,000 trials) with decreasing imaging noise (δu = 0.024, 0.016, 0.008, 0.004 mm). The result indicates that the distribution broadens with a higher mode and a heavier tail as the noise increases. When δu = 0.016 mm, f_0 reaches a value less than 3×10^{-4} around 70% of the time, which indicates that the yielding rate of the experiment-driven process within 15 iterations is around 70%.

As a result of the stochasticity and noise in the experiment, for example, when targeting Shape IV

(Extended Data Fig. 5), the gradient-descent search algorithm occasionally fails to reach the desired loss value of 0.005f(**V** = **0**) within 15 iterations. While gradient-based solvers are more efficient for a convex problem with minimal noise, global solvers help avoid becoming trapped in a local solution when noise is pronounced, or when the problem is clearly non-convex. Extended Data Fig. 4d–f provides an investigation of a typical global solver, the pattern search algorithm (Matlab, Global Optimization Toolbox, Pattern Search Options), in comparison with the gradient-descent algorithm, using the model-driven simulation of a 4×4 sample morphing into Shape IV. Extended Data Fig. 4d shows the simulation results with the objective function subjected to typical experimental noise and constraints (δu = 0.016 mm, 12-bit PWM output, and a maximum current I_{max} = 27 mA). The pattern search algorithm requires around six times more function evaluations than the gradient-based method to reach a loss value of 0.005f(**V** = **0**). When releasing the limitation on the maximum number of iterations, both algorithms can find a minimum loss of 0.0006f(**V** = **0**) within 20,000 function evaluations (Extended Data Fig. 4e). Extended Data Fig. 4f compares the algorithms in the case with 10 times higher 3D imaging noise (δu = 0.16 mm). While gradient descent method gets trapped in a local solution with a loss of 0.08f(**V** = **0**), pattern search method can find the same minimum (0.0006f(**V** = **0**)) as the case with lower noise.

The 2×2 mesh structure shown in Fig. 4a and the optical function shown in Fig. 5d exhibit nonlinear input-output relationships, such that convexity cannot be guaranteed. However, given the objective functions and constraints prescribed, the experiment-driven process does not run into any local solutions.

S6.3 Speed of the feedback control and optimization

Supplementary Table 1 lists the detailed, representative time budget of each step to complete one function evaluation for the experiment-driven optimization of a 4×4 sample. A remote computer takes an average of 0.06 s to send the updated values to the peripheral Raspberry Pi to update the voltage output of 16 PWM channels. The algorithm pauses 0.1 s to wait for the sample to settle to its steady state upon

actuation. The 3D imaging process consists of three consecutive steps: taking images of the sample from the stereo cameras (0.08 s), detecting locations of the nodes in the two images using OpenCV-Python *matchTemplate* function (0.11 s), calculating the 3D-recontructed nodal displacements using OpenCV-Python *reprojectImageTo3D* function (0.00 s). It takes a total of 0.19 s to get one feedback from 3D imaging. The remote computer runs the optimization algorithm (0.00 s). Overall, the time expenditure for each loss function evaluation cycle is ~0.35 s. Based on the experimental observation, a 4×4 sample takes an average of ~2.5 min to morph a shape from the zero-actuation initial state.

Supplementary Note S7: Approaches to increase the number of voltage inputs

S7.1 Scalability of the square-lattice *N*×*N* sample

In principle, the number of voltage inputs $4N$ of a $N \times N$ metasurface with a fixed size can increase by reducing the unit-cell size L_N. A single-conductive-layer structure with an overall size of L ultimately accommodates a maximum of $4L/L_N$ ports at its 1-dimensional boundary. Given L, increasing N will provide higher spatial resolution (Nyquist-Shannon sampling theorem). Advanced manufacturing techniques allow feature sizes (*e.g.*, ribbon widths) of the serpentine beams to be reduced by 1~2 orders of magnitude[S4], such that L_N can be scaled down to ~100 μm. Meanwhile, the overall size L can scale up easily as the fabrication process is compatible with the well-developed, wafer-based thin-film manufacturing technology. For example, a design with L = 100 mm (on a 6' wafer) and L_N = 100 μm can support 4×10^3 voltage inputs ($N = 10^3$).

S7.2 Hexagonal lattice

A more space-efficient design of the serpentine network can increase the number of controls, without changing the overall size L or the unit cell size L_N. Supplementary Fig. 28a, b shows that a hexagonal-

lattice structure of approximately the same overall/unit-cell sizes as the 4×4 square-lattice structure, can accommodate a factor of two increase in number of voltage inputs (34 vs. 16 ports). The additional number of voltage inputs enhance the range of target shapes that can be morphed with sufficiently small error (<2%), as exemplified in Supplementary Fig. 28c, d for a representative targeting subspace of 3D surfaces.

S7.3 Multilayer electrodes and hierarchical structures

Multilayer electrodes can further increase the maximum number of voltage inputs. Integrating hierarchical metasurface structures ($l \times l$ patches, with $l<L$) to increase the length of the control boundaries (from $4L$ to $4L^2/l$) will also boost the number of available input ports.

Supplementary Note S8: The abstract target curves and surfaces

The target curve in Supplementary Fig. 14c is a segment of arc, with the following expression

$$\mathrm{Z} = \sqrt{r^2 - X^2} - (r - c),\ r = \frac{L^2 + 4c^2}{8c}. \tag{S10}$$

c = 0.1L leads to the particular shape in Supplementary Fig. 14c. The target curve in Supplementary Fig. 14d is a sinusoidal function $Z = -c\sin\left(\frac{2\pi X}{L}\right)$. c = 0.15 L leads to the particular shape in Supplementary Fig. 14d.

The target shapes in the dynamic process in Fig. 1d, and the shapes studied in Fig. 3 and Extended Data Fig. 5 are defined by the following functions, with Z denoting the out-of-plane coordinate, and X and Y denoting the in-plane coordinates.

Function 1

$$r = \frac{a^2 + c^2}{2c}$$
$$Z = \begin{cases} \sqrt{r^2 - X^2 - Y^2} - (r - c) & \sqrt{X^2 + X^2} \le a \\ 0 & \sqrt{X^2 + Y^2} > a \end{cases}. \tag{S11}$$

The 'rising up' process is simulated by $a = 0.5L$ and c increasing from 0 to $0.3L$. Shape I in Extended Data Fig. 5 is defined by $a = 0.5L$ and c = $0.2L$.

Function 2

$$Z = c\exp\left[-\frac{\left(X - X_{\mathrm{c}}\right)^2 + \left(Y - Y_{\mathrm{c}}\right)^2}{a^2}\right]. \tag{S12}$$

The 'moving around' process in Fig. 1d is simulated by $c = 0.2L$, $a = 0.4L$, and changing X_{c} and Y_{c} such that the point with the maximum Z- coordinate moves along a path in the XY plane. The prescribed path in Fig. 1d starts at (X_{c}, Y_{c}) = (0, 0), moves to ($0.2\sqrt{2}\,L$, 0), moves circularly with $\sqrt{X_{\mathrm{c}}^2 + Y_{\mathrm{c}}^2} = 0.2\sqrt{2}L$, and then back to (0, 0). Shape II in Extended Data Fig. 5 is defined by $X_{\mathrm{c}} = Y_{\mathrm{c}} = 0.2L$, $a = 0.4L$, and $c = 0.2L$. The target shapes in Supplementary Fig. 29b are defined by $X_{\mathrm{c}} = Y_{\mathrm{c}} = 0$ and varying parameters a and c.

Function 3

$$Z = \sum_{i=1,2} c_i \exp\left\{-\frac{\left[X + (-1)^i X_{\mathrm{c}}\right]^2 + \left[Y + (-1)^i Y_{\mathrm{c}}\right]^2}{a^2}\right\}. \tag{S13}$$

The first a few shapes of the 'splitting up' process in Fig. 1d is simulated by $c_1 = c_2 = 0.2L$, $a = 0.32L$, and X_{c} and Y_{c} changing from 0 to $0.2L$, with the last one denoted by shape A. Each shape is scaled such that the maximum Z coordinate is $0.2L$. The last shape of the 'splitting up' process (shape B) is simulated by $c_1 = -c_2 = 0.1L$, $a = 0.4L$, and $X_{\mathrm{c}} = Y_{\mathrm{c}} = 0.25L$. A few shapes are added between shape A and B by interpolating the two shapes to make the process continuous. The 'oscillating' process in Fig. 1d is simulated by $X_{\mathrm{c}} = Y_{\mathrm{c}} = 0.25L$, $a = 0.4L$, $c_1 = -c_2$, and c_1 changing periodically between $-0.1L$ and $0.1L$. The target shape in Fig. 3, the same as Shape III in Extended Data Fig. 5, is defined by $X_{\mathrm{c}} = Y_{\mathrm{c}} = 0.2L$, $a = 0.4L$, and $c_1 = -c_2 = 0.1L$.

Function 4

$$Z = \sum_{\substack{i=1,2 \\ j=1,2}} (-1)^{i+j} c\exp\left\{-\frac{\left[X + (-1)^i X_{\mathrm{c}}\right]^2 + \left[Y + (-1)^j Y_{\mathrm{c}}\right]^2}{a^2}\right\}. \tag{S14}$$

Shape IV in Extended Data Fig. 5 is defined by $X_{\mathrm{c}} = Y_{\mathrm{c}} = 0.25L$, $a = 0.4L$, and $c = 0.1L$.

Function 5

$$Z=\begin{cases}\frac{c}{2}\left[\cos\left(\frac{\pi X}{a}\right)+1\right] & |X|\le a\\ 0 & |X|>a\end{cases}. \qquad \text{(S15)}$$

Shape V in Extended Data Fig. 5 is defined by a = 0.5L and c = 0.2L.

Function 6

$$X'=\frac{\sqrt{2}}{2}X+\frac{\sqrt{2}}{2}Y,\ Y'=-\frac{\sqrt{2}}{2}X+\frac{\sqrt{2}}{2}Y$$
$$Z=\begin{cases}\frac{c}{2}\left[\cos\left(\frac{\pi X'}{a}\right)+1\right] & |X'|\le a\\ 0 & |X'|>a\end{cases}. \qquad \text{(S16)}$$

Shape VI in Extended Data Fig. 5 is defined by a = 0.5L and c = 0.1L .

In addition to those shapes presented in the manuscript, the serpentine-shaped mesh structures may also be deformed to form a number of surfaces represented by the general forms of Functions 1–6, as studied in Supplementary Note S11.2.

Supplementary Note S9: Experimental characterization of an array of serpentine beams

Supplementary Fig. 14a shows a typical sample consisting of an array of N (N = 8) serpentine beams (sample length L = 10.4 mm, sample width W = 20.6 mm, column/vertical serpentine beam length L_N = 5.2 mm, row/horizontal serpentine beam length L_M = 2.52 mm). The horizontal serpentine beams are polyimide (PI) beams and are non-conductive. As a result, the sample has eight electrically controlled and mechanically coupled serpentine beams. A voltage vector (**V**) of size 16, applied to the peripheral ports (8 pairs of ports), controls the current density (**J**) in each beam. The displacements (u) of the intersections of adjacent serpentine beams (the nodes) define the outline of the deformed 2D shape. The displacement of the ith node, u_i, is approximately linearly related to the response of the ith node to each jth portal voltage, V_j, as follows:

$$u_i=\sum_{j=1}^{2N}C_{ij}V_j,\ \text{for } i=1,\dots N. \qquad \text{(S17)}$$

The coupling matrix **C** fully describes this approximately linear mechanical system driven by electromagnetic force. Supplementary Fig. 14b shows FEA and experimental characterization of the electro-magneto-mechanical behavior for representative nodes of the array sample provided voltages in the range of 0~2.5 V. A regression analysis on the FEA results (R^2~0.95) provides the coupling coefficients for a linear-system characterization. This linear approximation enables a model-driven approach that optimizes the portal voltages for the precursor array to deform to a mathematically-defined target shape. Supplementary Fig. 14c, d shows the morphing results of the sample targeting spherical and sinusoidal shapes.

Supplementary Note S10: Definition of the error between deformed and target shapes

For the deformed array of *N* serpentine structures, a continuous 2D curve $Z^{\mathrm{Deform}}(X)$ can be constructed from the nodal positions u_n (n = 0~N+1, $u_0 = u_{N+1} = 0$) via interpolation. The error between this deformed 2D curve and the target curve $Z(X)$ is then defined as

$$\mathrm{Error} = \frac{1}{L}\sqrt{\frac{1}{L}\int_{-L/2}^{L/2}\left[Z^{\mathrm{Deform}}(X) - Z(X)\right]^2 \mathrm{d}X}\,. \tag{S18}$$

Similarly, for the deformed $N \times N$ mesh structure, a continuous 3D surface $Z^{\mathrm{Deform}}(X,\ Y)$ can be constructed from the nodal displacements u_n^m (m = 0~N+1, n = 0~N+1, $u_n^0 = u_n^{N+1} = u_0^m = u_{N+1}^m = 0$) via interpolation. The error between this deformed 3D surface and the target surface $Z(X,\ Y)$ is then defined as

$$\mathrm{Error} = \frac{1}{L}\sqrt{\frac{1}{L^2}\int_{-L/2}^{L/2}\int_{-L/2}^{L/2}\left[Z^{\mathrm{Deform}}(X,\ Y) - Z(X,\ Y)\right]^2 \mathrm{d}X\mathrm{d}Y}\,. \tag{S19}$$

Supplementary Note S11: A numerical study on the feasible range of target shapes

To illustrate that the same mesh structure can be deformed to form abundant target shapes, a numerical study is presented in this Supplementary Note on the error (see Supplementary Note 10 for the definition) of

the deformed shape for a few classes of target shapes in general form.

S11.1 Target 2D curves

For functions defined in the range $-L/2 \le X \le L/2$ and taking the form $Z = A_1\left[\cos\left(\frac{2\pi X}{L}\right)+1\right] + A_2\left[\cos\left(\frac{4\pi X}{L}\right)-1\right]$, changing the parameters A_1 and A_2 leads to various target 2D curves. The model-driven approach can be applied for the same precursor structure to form many of these 2D curves. The error of the shapes formed by the array of 8 serpentine beams presented in Supplementary Fig. 14 is shown in the contour plot of Supplementary Fig. 20a. When the parameters A_1/L and A_2/L are in a wide range, the error is less than 2%, indicating that a number of target curves can be approximated by the deformed structure quite accurately. This error mainly comes from the limitation on the electric current to avoid temperature change from Joule heating (I < 27.5mA), which limits the ability to form target shapes that require large deformation.

The above target curves are symmetric with respect to the vertical axis at X = 0. Similarly, the asymmetric target 2D curves defined in the range $-L/2 \le X \le L/2$ and taking the form $Z = B_1\sin\left(\frac{2\pi X}{L}\right) + B_2\sin\left(\frac{4\pi X}{L}\right)$ can also be formed by the mesh structure quite accurately when B_1/L and B_2/L are in a wide range (Supplementary Fig. 20b).

In a more general case, a target 2D curve $Z(X)$ defined in the range $-L/2 \le X \le L/2$ with $Z(\pm L/2) = 0$ may be expressed by the Fourier series as

$$Z = \sum_{k=1}^{Q} A_k\left[\cos\left(\frac{2k\pi X}{L}\right)+(-1)^{k-1}\right] + \sum_{k=1}^{Q} B_k\sin\left(\frac{2k\pi X}{L}\right). \qquad \text{(S20)}$$

The prior study applies to the curves that are symmetric (B_k = 0) or asymmetric (A_k = 0) with respect to the vertical axis at X = 0 and are dominated by the first two terms ($A_{k>2} \approx 0$ and $B_{k>2} \approx 0$). The curves that involve higher order terms may be formed by the structure with more serpentines (*i.e.,* larger N). Supplementary Fig.

21 shows that the array of 16 serpentine beams may form target curves in a wide range with order Q = 4 in the Fourier series.

S11.2 Target 3D surfaces

For functions defined in the range $-L/2 \le X,\ Y \le L/2$ and taking the form defined by Function 1 (Eq. (S11)) in Supplementary Note S8, changing the parameters *a* and *c* leads to various target 3D surfaces. The model-driven approach can be applied for the same precursor structure to form many of these 3D surface. The error of the shapes formed by the 4 × 4 mesh structure presented in the main text is shown in the contour plot of Supplementary Fig. 22. When the parameters *a*/*L* and *c*/*L* are in a wide range, the error is less than 2%, indicating that a number of target surfaces can be approximated by the deformed mesh structure quite accurately. Similar analysis is performed to the target 3D surfaces defined by Function 2~6 (Eqs. (S12)–(S16)) in Supplementary Note S8, showing that the same mesh structure can be deformed to various target shapes accurately (Supplementary Figs. 23–27).

Supplementary Note S12: Shape morphing in time-varying, non-uniform magnetic fields

S12.1 Spatiotemporal control of the shape of a serpentine beam

A time-dependent, non-uniform magnetic field enables precise spatiotemporal control of the local deformation within a serpentine beam. Extended Data Fig. 3a-c shows refined shape-morphing of a single serpentine beam (H = 1.2 mm, h_{PI} = 7.5 μm) conducting a current of 20 mA and placed in a non-uniform, time-varying magnetic field produced by a small, moving magnet. The small disk-shaped magnet (diameter D = 11.0 mm, thickness h = 5.0 mm, surface field B = 481.6 mT; D73-N52, K&J Magnetics, Inc.), placed 3.0 mm below the center of the beam (ΔZ = -3 mm), generates a localized magnetic field around its instant position. By varying the position of the magnet along the *X*-axis, the deformed structure is dragged in the

opposite direction of ΔX, as illustrated in Extended Data Fig. 3b. Extended Data Fig. 3c shows a skewed shape of the beam with the peak Z-axis displacement (Z_{max}) shifting along the Y-axis while moving the magnet in the same direction. In a uniform magnetic field, asymmetric shape morphing of a single beam structure is impossible as the beam always conducts a uniform current.

S12.2 4×4 sample morphing into a donut-like shape in a non-uniform magnetic field

A changing field and field gradient can provide extra degrees of spatiotemporal control of the electromagnetic response. Extended Data Fig. 3d shows a design for a non-uniform magnetic field generated by adding a small magnet 3.0-mm below the center of the 4×4 sample in the existing setup. Measurements of the magnetic flux density using a gaussmeter (GMHT201, Apex Magnets) shows a superposition of a magnetic field to the original field in the center, ~5.0 mm-diameter area (Extended Data Fig. 3e). Intuitively, the additional, localized magnetic field facilitates morphing of the metasurface into target shapes with localized deformation around the center of this additional field. Extended Data Fig. 3f shows experimental results of the 4×4 sample morphing into a donut-like target shape via experiment-driven self-evolving process in both uniform and non-uniform magnetic field. Both experiment and noise-free simulation show that the metasurface cannot morph into the donut-like shape with sufficiently small error (e < 2%) in a uniform magnetic field. In contrast, the non-uniform field environment allows this shape by enhancing negative out-of-plane deformation close to the center while maintaining the positive displacements far from the center.

S12.3 FEA and numerical studies on the shape morphing in a non-uniform magnetic field

FEA and numerical studies investigate the accessible range in subspaces of 3D surfaces and demonstrates an enhanced morphing capability due to an alterable, non-uniform magnetic field.

Supplementary Fig. 29a shows a design of a non-uniform magnetic field, $\boldsymbol{B}_{\text{local}} + \boldsymbol{B}_{\text{far}}$, where $\boldsymbol{B}_{\text{local}}$ is generated by a small magnet (M=1.1×10^6 A/m, magnetization along the diagonal direction in XY plane, see Supplementary Note S2.1) 2 mm below the center of the 4×4 structure and $\boldsymbol{B}_{\text{far}}$ is a uniform magnetic field. To simulate a time-varying magnetic field, $\boldsymbol{B}_{\text{local}}$ and $\boldsymbol{B}_{\text{far}}$ can be independently turned on or off. Local magnetic field $\boldsymbol{B}_{\text{local}}$ facilitates morphing of the metasurface into target shapes with localized deformation around the center of the small magnet. Examples are the Gaussian shapes in the form, $Z = c\exp\left(-\frac{X^2+Y^2}{a^2}\right)$, when a is much smaller than the overall size L. Supplementary Fig. 29b shows that in a localized magnetic field $\boldsymbol{B}_{\text{local}}$ ($\boldsymbol{B}_{\text{far}} = \boldsymbol{0}$), the range of the above Gaussian shapes that can be morphed into with sufficient accuracy is wider than that in a uniform magnetic field $\boldsymbol{B}_{\text{far}}$ ($\boldsymbol{B}_{\text{local}} = \boldsymbol{0}$). Supplementary Fig. 29c shows a similar investigation but on another targeting subspace, with the targeting shapes in the form, $Z = a\left[\cos\left(\frac{2\pi(\sqrt{X^2+Y^2})}{L}\right)+1\right] + c\left[\cos\left(\frac{4\pi(\sqrt{X^2+Y^2})}{L}\right)-1\right]$. Compared to the case in a uniform magnetic field $\boldsymbol{B}_{\text{far}}$, the range of producible shapes reshapes upon the introduction of a non-uniform magnetic field $\boldsymbol{B}_{\text{local}} + \boldsymbol{B}_{\text{far}}$, rather than simply expands.

Supplementary Note S13: Computational cost for the model-driven approach

S13.1 Linear system

For the $N\times N$ array of serpentine structures presented in the main text, there are $4N$-1 independently controlled port voltages V_1, V_2, …, V_{4N-1} (one port is connected to ground and always has zero voltage). FEA can be performed to establish the relationship between node displacements and port voltages. Applying voltage V_j at port j and keeping the voltages of other ports being zero, FEA predicts the deformation and an approximate linear fitting of the nodal displacements gives $u_i = C_{ij}V_j$. To obtain the coefficient C_{ij} for all voltages, FEA is performed $4N$–1 times, each time for j=1, 2, …, $4N$–1. When all the port voltages are applied simultaneously, the nodal displacements are the superposition of those when the voltage is applied individually due to linearity, *i.e.*, $u_i = \sum_{j=1}^{4N-1} C_{ij}V_j$, such that the nodal displacements can be evaluated rapidly

without additional FEA. Therefore, the total number of FEA scales linearly with the system size N, which is acceptable.

S13.2 Nonlinear system

For a nonlinear system, the above linear superposition approach is no longer valid and the nodal displacements are nonlinear functions of the port voltages, *i.e.*, $u_i = G_i\left(V_1, V_2, ...V_{4N-1}\right)$. Taking *P* values for each voltage, P^{4N-1} times of FEA is needed to obtain the nonlinear function G_i, which is astronomical (*e.g.*, *P* = 5 and *N* = 2 lead to $P^{4N-1} \approx 7.8\times10^4$). For the 2×2 array (*N* = 2) presented in the manuscript, each FEA takes about 1 hour using a workstation (twenty-core, 2.4GHz processor, 64GB memory). This difficulty in the model-driven strategy based on computation is common for nonlinear systems.

Supplementary Note S14: Characterization of the resolution and uncertainty of 3D imaging

Supplementary Fig. 30a is a schematic illustration of the experimental setup for characterization of the resolution and uncertainty of the 3D imaging method. In the setup, a side camera (Webcams, ELP, 3840×2160-pixel resolution, 30 fps) provides direct imaging of the out-of-plane deformation. Analyzing the images via ImageJ 1.x pipeline gives the ground-truth measurement of the nodal displacement (u_{m}). Two cameras (Webcams, ELP, 3840×2160-pixel resolution, 30 fps) are placed symmetrically side-by-side above the sample to take top-view images. A calibration algorithm (OpenCV-Python *calibrateCamera* function) is applied to a collection of checkerboard images (custom-made, 7×8 squares, 2×2 mm per square) to correct lens distortion[S5]. The sample nodes provide distinctive cross geometry for image registration. A customized template matching algorithm (based on OpenCV-Python *matchTemplate* function) returns the nodal coordinates ([x_1, y_1] and [x_2, y_2]) from the pair imaging in units of pixels (px). A perspective projection matrix[S6] transforms the disparity ($D(x,y) = \sqrt{(x_1-x_2)^2+(y_1-y_2)^2}$) at the estimated location ([$x = (x_1+x_2)/2$, $y = (y_1+y_2)/2$]), to the relative depth between the camera plane and the node, $Z(X,\ Y)$, as,

$$\begin{bmatrix} X \\ Y \\ Z \\ 1 \end{bmatrix} = \begin{bmatrix} 1 & 0 & 0 & 0 \\ 0 & 1 & 0 & 0 \\ 0 & 0 & bf' & 0 \\ 0 & 0 & 0 & 1 \end{bmatrix} \begin{bmatrix} x \\ y \\ 1/D(x,y) \\ 1 \end{bmatrix}, \quad \text{(S21)}$$

where f'= 35 mm is the focal length of the cameras, b = 85 mm is the distance between the two cameras. A transformation algorithm (based on OpenCV-Python *reprojectImageTo3D* function) implements this 2D-to-3D projection and predicts the nodal depth in a unit of pixels (px) as $u_p = Z(X, Y)$.

A cycling test on a 4×4 sample (200 actuation cycles of Shape IV in Extended Data Fig. 5, at a frequency of 1 Hz) provides a statistical analysis of the 3D-reconstructed depth measurement (u_p). The results show the mean values and standard errors of u_p from 200-cycle measurement for the 16 nodes. The distribution of the measured depth (u_p) at node 1 of the actuated/unactuated state follow a Gaussian distribution with a standard deviation of ~0.25. A statistical analysis of u_p measured from all 16 nodes yields a standard deviation, δu_p = 0.25 px (Supplementary Fig. 30b). The side camera measurement (u_m) has an uncertainty, $\delta u_m \approx \pm 0.015$ mm. Supplementary Fig. 30c shows a linear relation between u_p and u_m predicted by a Deming regression on the experimental data as $u_m = au_p + b$, where a = -0.0664 ± 2.543×10^{-4}, b = 12.05 ± 0.038 (R^2 ~0.997). The regression model defines the 3D-reconstructed nodal displacement, The regression model defines the 3D-reconstructed nodal displacement, $u(u_p) = u_m(u_p)$. Given au_p (resolution of u_p = 0.1 px) refers to resolution and $a\delta u_p + \delta b$ evaluates the uncertainty, the uncertainty nodal displacement (u) measured by 3D imaging method has a resolution of ~0.006 mm and an uncertainty of ±0.055 mm.

The pixel form measurement of the X-Y coordinates can be converted to physical values given a reference scale bar. Renka-Cline gridding matrix method produces an interpolated 3D surfaces from the reconstructed nodal displacement $u(X, Y)$ at three inserted query points between the two nearest nodes.

Supplementary Note S15: Self-evolving of a nonlinear system

A 2×2 sample (L = W = 25.0 mm, L_N = L_M = 10.25 mm), consisting of serpentine beams without straight segments connecting the semi-circle parts, represents a metasurface that exhibits an amplified non-linear

mechanical behavior in response to the voltage inputs. Compared to that in the 4×4 and 8×8 sample, the arc length (distance between two ends along the section of the curve) of each serpentine beam is largely reduced. Extended Data Fig. 7 a–d shows the side-view images of the sample deforming out-of-plane given an increasing voltage to port 1 (Fig. 4d). Centered in the same magnetic setup, with the increase of the voltage input, the out-of-plane bending initially dominates the structure deformation but saturates at a small displacement due to reduced arc length, such that the serpentine beams need to overcome the tensile rigidity much larger than the bending rigidity for further deformation. The goodness of fit (R^2) of a linear regression on this response (for model-driven approach) is ~0.8. In the experiment-driven approach, the optimization takes a loss function and stopping criteria of the same form as the 4×4 sample.

Supplementary Note S16: Self-evolving towards multifunctionality

Fig. 5c shows the illustration of a 3×3 sample (L = W = 14.8 mm, L_N = L_M = 4.06 mm) with 9 reflective gold patches (Au, 2 mm × 2 mm in size, 300 nm in thickness) mounted on the nodes. The receiving screen (white printer paper, 55 mm × 80 mm) is placed 40 mm above the sample in parallel to the XY-plane. A red laser beam (~650 nm in wavelength and ~1 mm in beam diameter) and a green laser beam (~520 nm in wavelength and ~1 mm in beam diameter) hit the center of two patches separately and got reflected. A top camera (Webcams, ELP, 3840×2160-pixel resolution, 30 fps) monitors the reflected laser spots on the receiving screen. The target optical function is to overlap two laser spots on the receiving screen. A customized imaging analysis method detects the centroid coordinates of the red/green laser spots as their current locations on the screen ([$x^{r/g}$, $y^{r/g}$], Extended Data Fig. 9a). The target structural function is to keep central nodal displacement at -0.5 mm (u_5^* = -0.5 mm). A linear model for the sample (provided by FEA) virtually monitors u_5 given the applied voltages. A post analysis via ex-situ 3D imaging shows an agreement between the model prediction and the experimental results.

A loss function $f_{\mathrm{multi}}(\boldsymbol{V})$ (Entended Data Fig. 9b), tailored for the target multifunctionality, is a linear

combination of two parts,

$$f_{\text{multi}}(\boldsymbol{V}) = af_{\text{opt}}(\boldsymbol{V}) + bf_{\text{struct}}(\boldsymbol{V}), \quad \text{(S22)}$$

where $f_{\text{opt}}(\boldsymbol{V})$ evaluates the distance between the two reflected laser spots, and $f_{\text{struct}}(\boldsymbol{V})$ evaluates the central nodal error, both normalized to have an initial value of 1 following,

$$f_{\text{opt}}(\boldsymbol{V}) = \frac{(x^r - x^g)^2 + (y^r - y^g)^2}{(x_0^r - x_0^g)^2 + (y_0^r - y_0^g)^2}, \quad \text{(S23)}$$

$$f_{\text{struct}}(\boldsymbol{V}) = \left(\frac{u_5 - u_5^*}{u_5^*}\right)^2, \quad \text{(S24)}$$

where $[x_0^{r/g}, y_0^{r/g}]$ is the initial location of red/green spots on the screen. The two target functions are equally weighted with $a = b = 0.5$. The experiment-driven self-optimization takes the same algorithm and stopping criteria as the ones applied to the 4×4 sample.

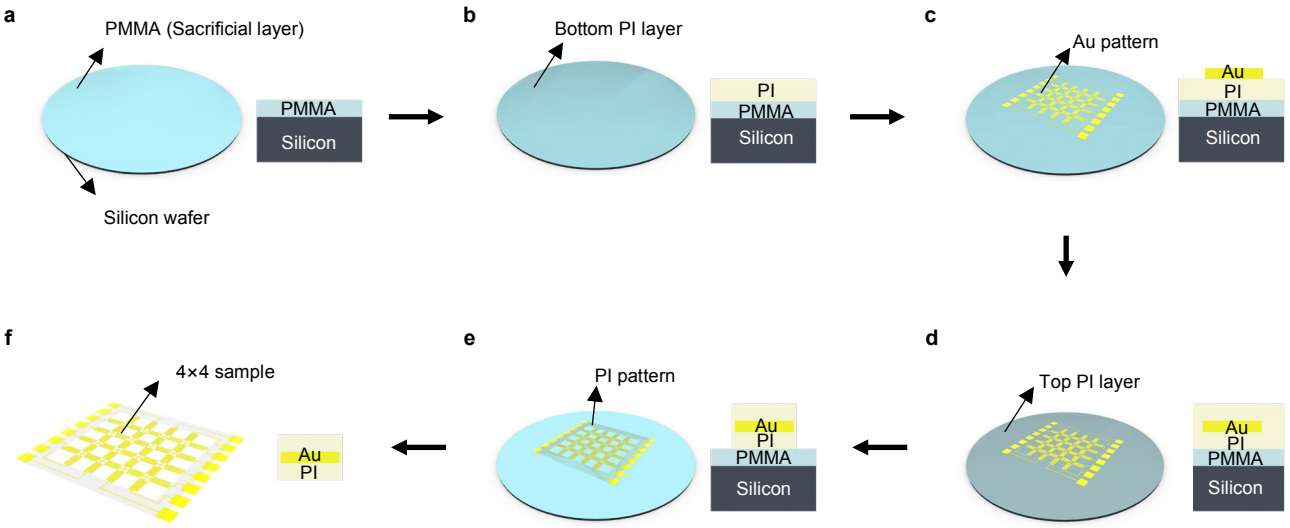

Supplementary Fig. 1 | Schematic illustration of the fabrication process. a, Prepare a sacrificial layer (PMMA) on a silicon wafer. **b,** Spin coat a bottom polyimide (PI) layer. **c,** Define the gold (Au) pattern. **d,** Spin coat the top PI layer. e, Define the PI pattern. f, Undercut sacrificial layer to release the sample from the silicon wafer.

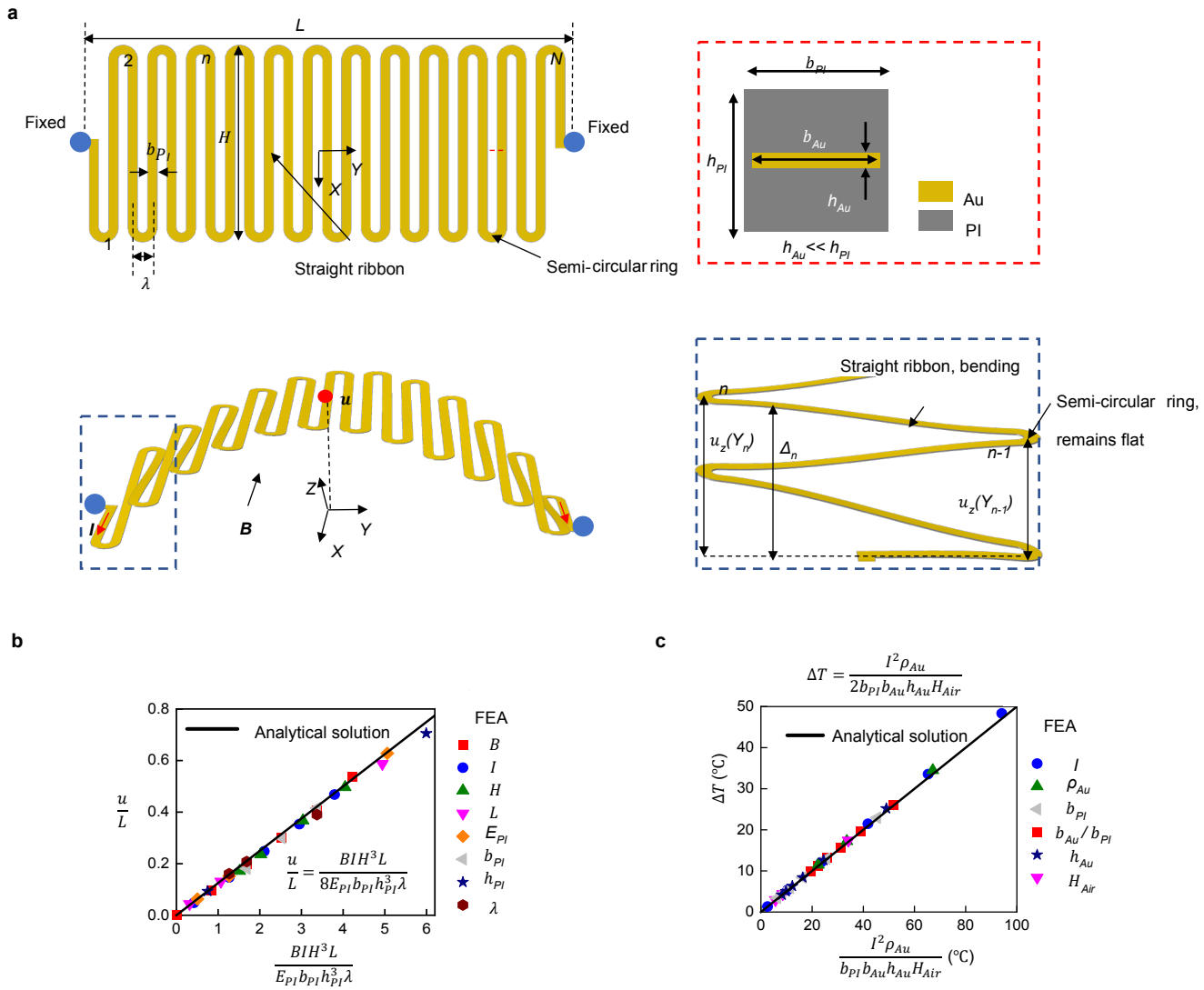

Supplementary Fig. 2 | An analytical model and FEA study of the mechanical and thermal behaviors of a single serpentine beam in response to electromagnetic actuation. a, Schematic illustration (top and cross-sectional views) of the initial state (top) and actuated state (bottom) of a serpentine beam. **b,** Analytical model and FEA study of the relationship of the maximum out-of-plane displacement u vs. the combination of electric current I, magnetic field B, material and geometry parameters. **c**, An analytical model of the temperature change due to Joule heating, compared with FEA study of the temperature change of the single serpentine beam.

a

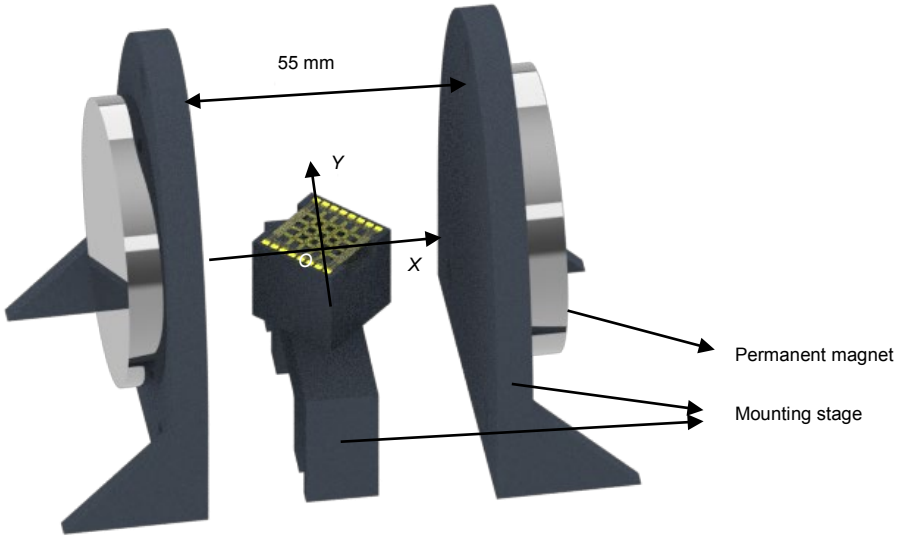

b

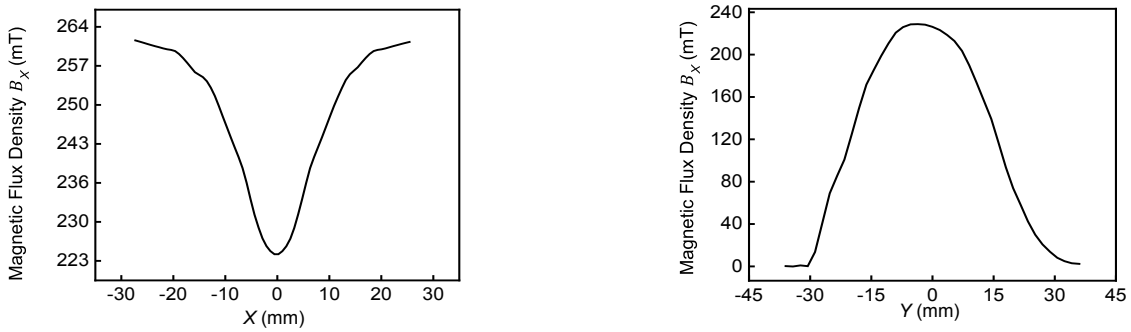

Supplementary Fig. 3 | Magnetic setup for Lorentz force actuation. a, Schematic illustration of the magnetic setup consisting of two parallel disks of Neodymium magnets (surface field ~264.0 mT) fixed on a 3D-printed mounting stage and spaced 55 mm apart. The setup generates a relatively uniform magnetic field of ~224 ± 16 mT in the center (*O*) and perpendicular to the disk plane (*X*-direction). **b,** The magnetic flux density in *X*-direction (B_X) measured by a gaussmeter (GMHT201, Apex Magnets) across the center (*O*) along *X-axis* and *Y-axis*. The model-driven process considers the magnetic field to be uniform with *B* = 224 mT and neglects the spatial variation.

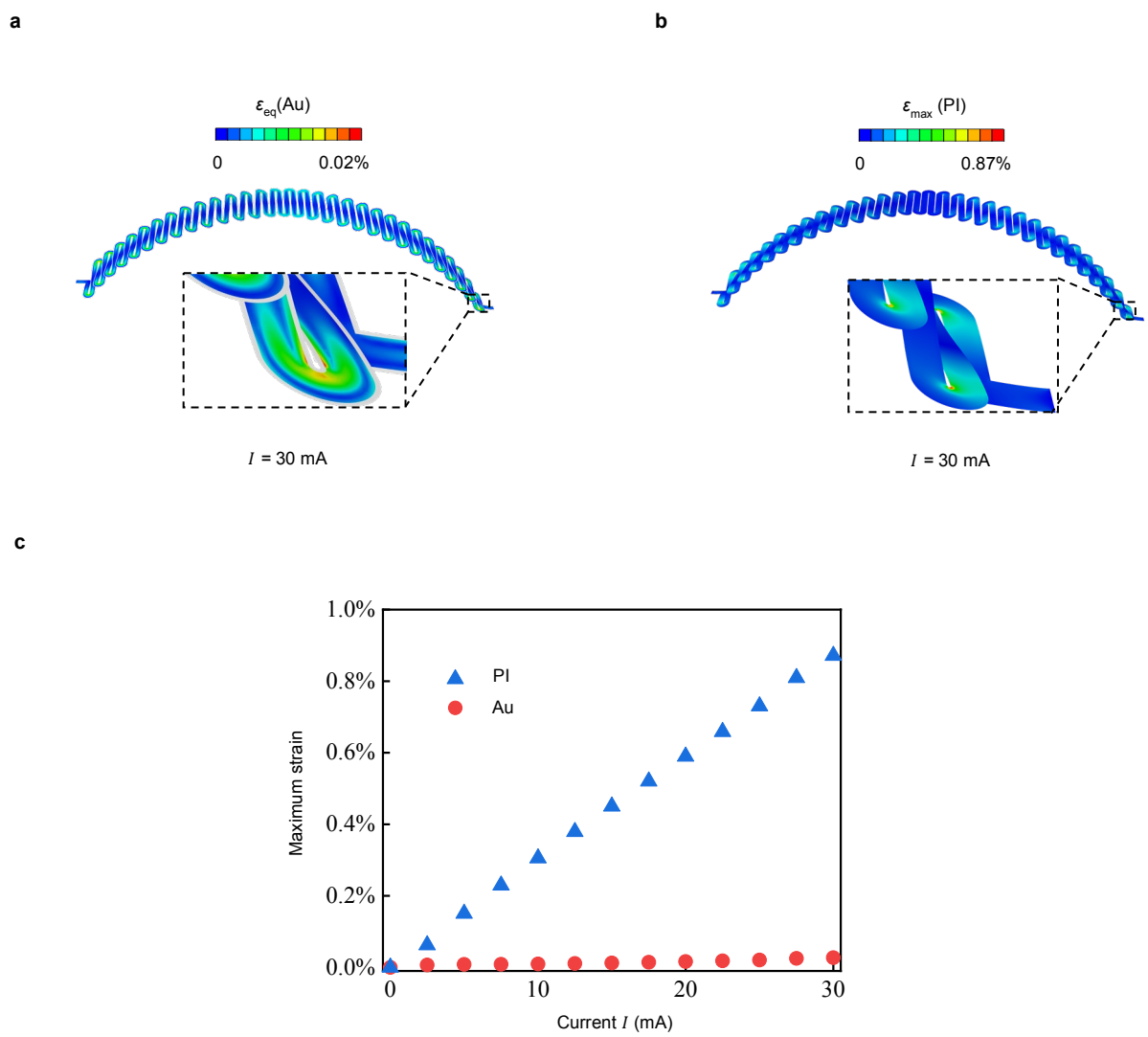

Supplementary Fig. 4 | FEA strain study on the deformed single serpentine beam. a, b, Distribution of the equivalent strain in Au (a) and the maximum principal strain in PI (b) when applied current I = 30 mA. **c,** The relationship of the maximum equivalent strain in Au and the maximum principal strain in PI vs. applied current I.

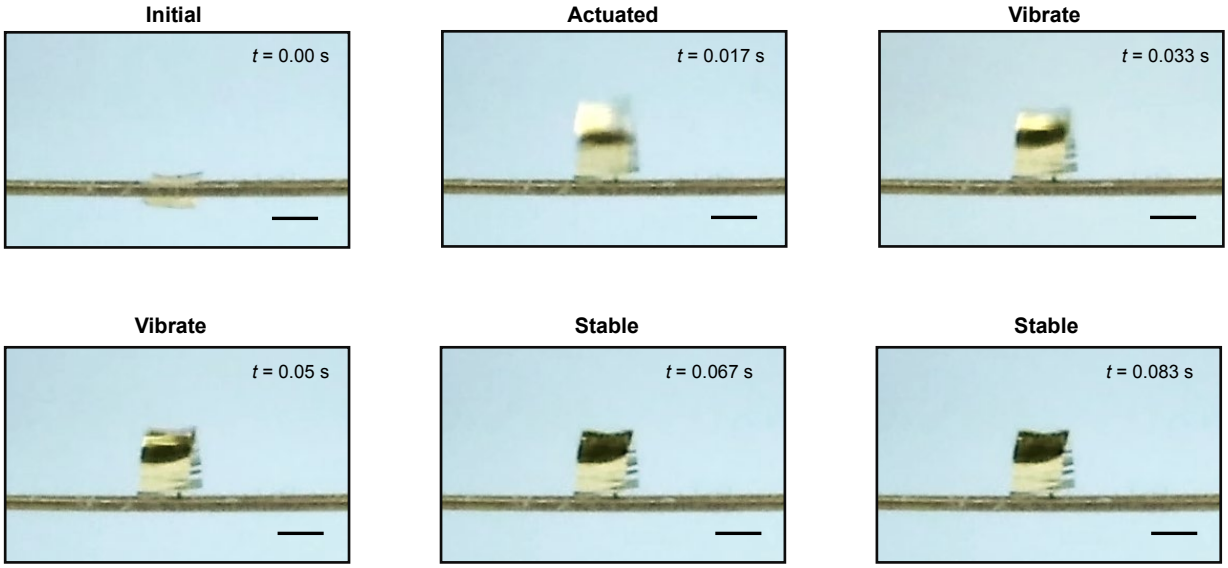

Supplementary Fig. 5 | Characterization of the response time of a single-beam sample. A single beam settles to steady state within ~0.07 s upon a step current actuation (applied current I = 10 mA). The dynamic process is monitored by a side camera (Canon EOS R, 60 fps). Scale bars, 1 mm.

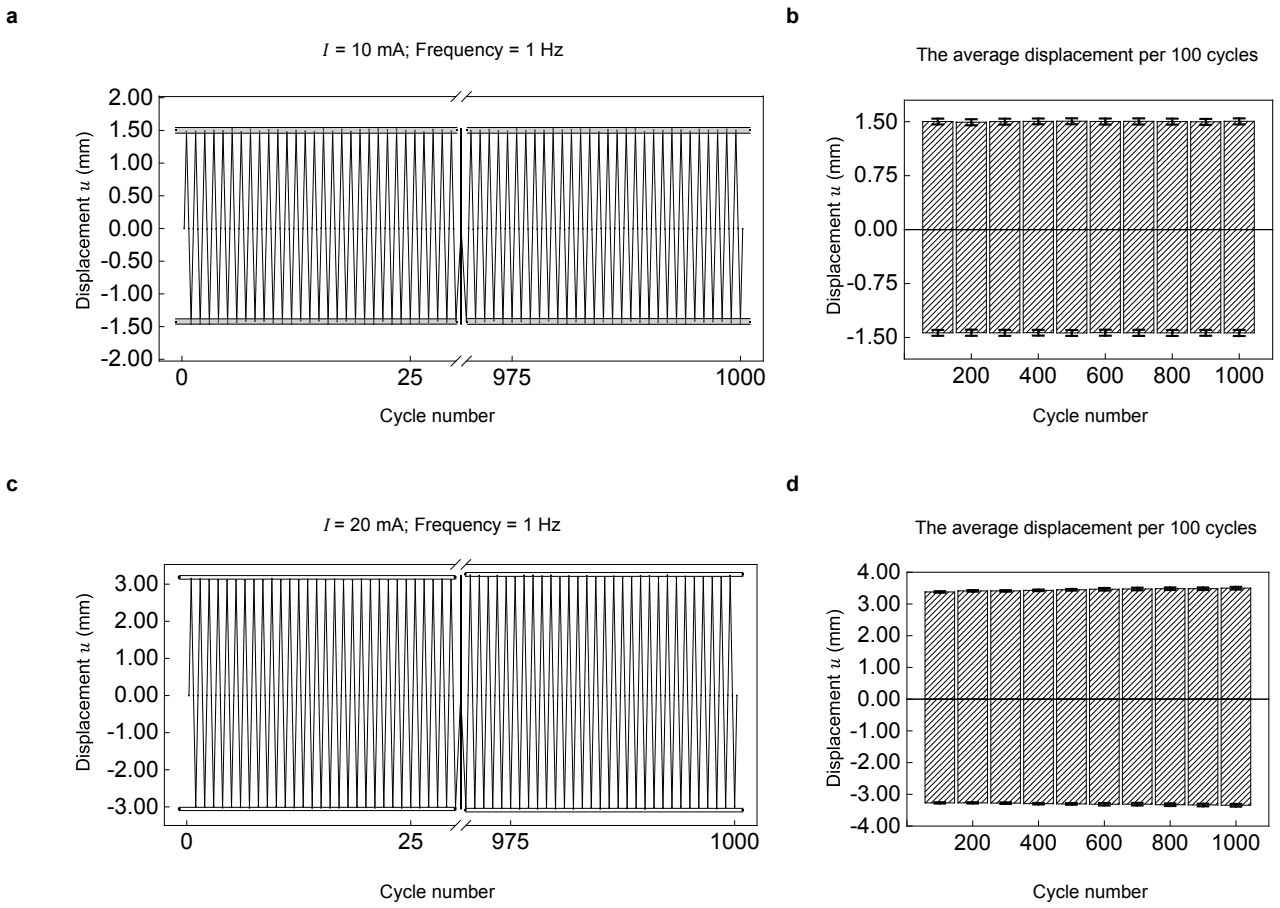

Supplementary Fig. 6 | Cyclic mechanical behavior of a single-beam sample. The displacement of the beam is monitored by a side camera (Canon EOS R, 60 fps) during 1000 actuation cycles at 1 Hz with current amplitude of ±10 mA (a, b) and ± 20 mA (c, d). Under large deformation (±20 mA) the displacement amplitude increases by ~4% post 1,000 cycles.

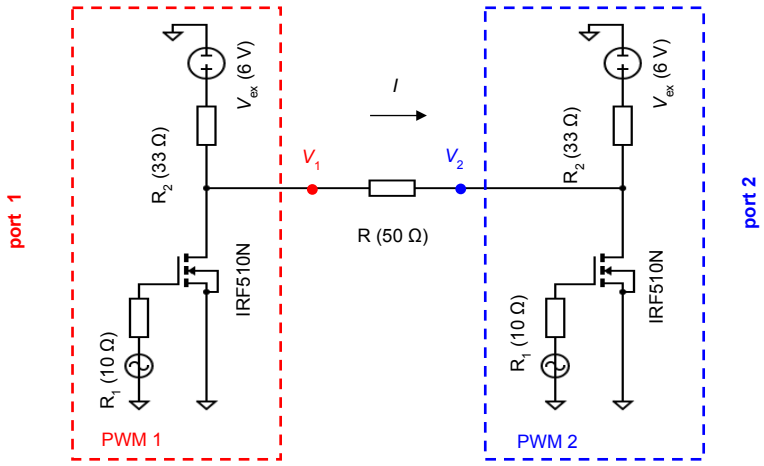

Supplementary Fig. 7 | Control and amplification circuits. A resistor of 50 Ω represents the impedance of the sample between two ports. Each PWM output signal is amplified by a MOSFET (Infineon Tech, IRF510N) provided by an external power supply (V_{ex} = 6 V).

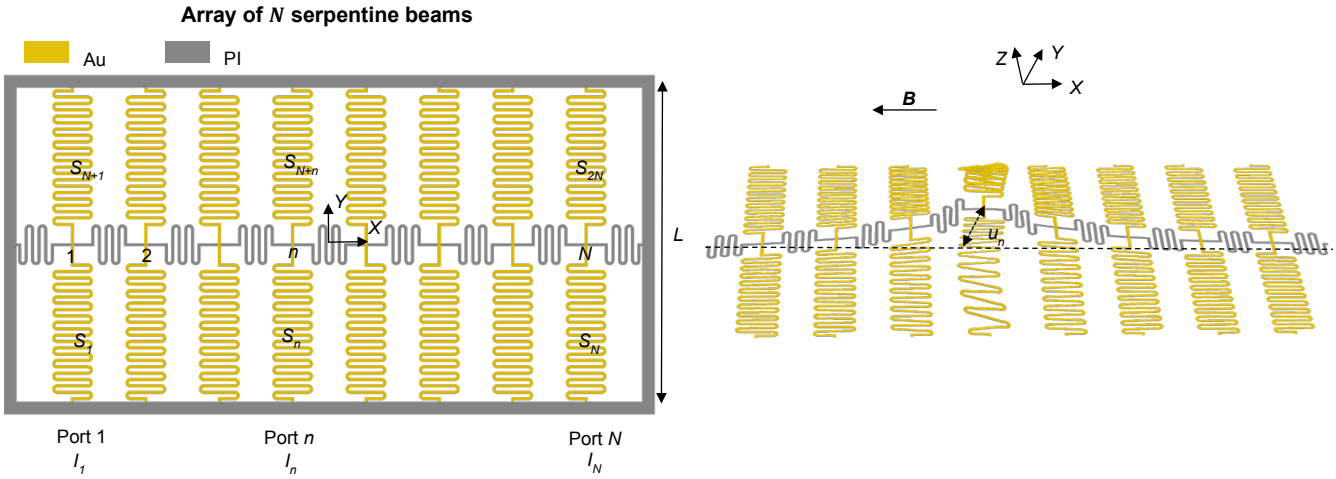

Supplementary Fig. 8 | Schematic illustration of an array of *N* serpentine beams.

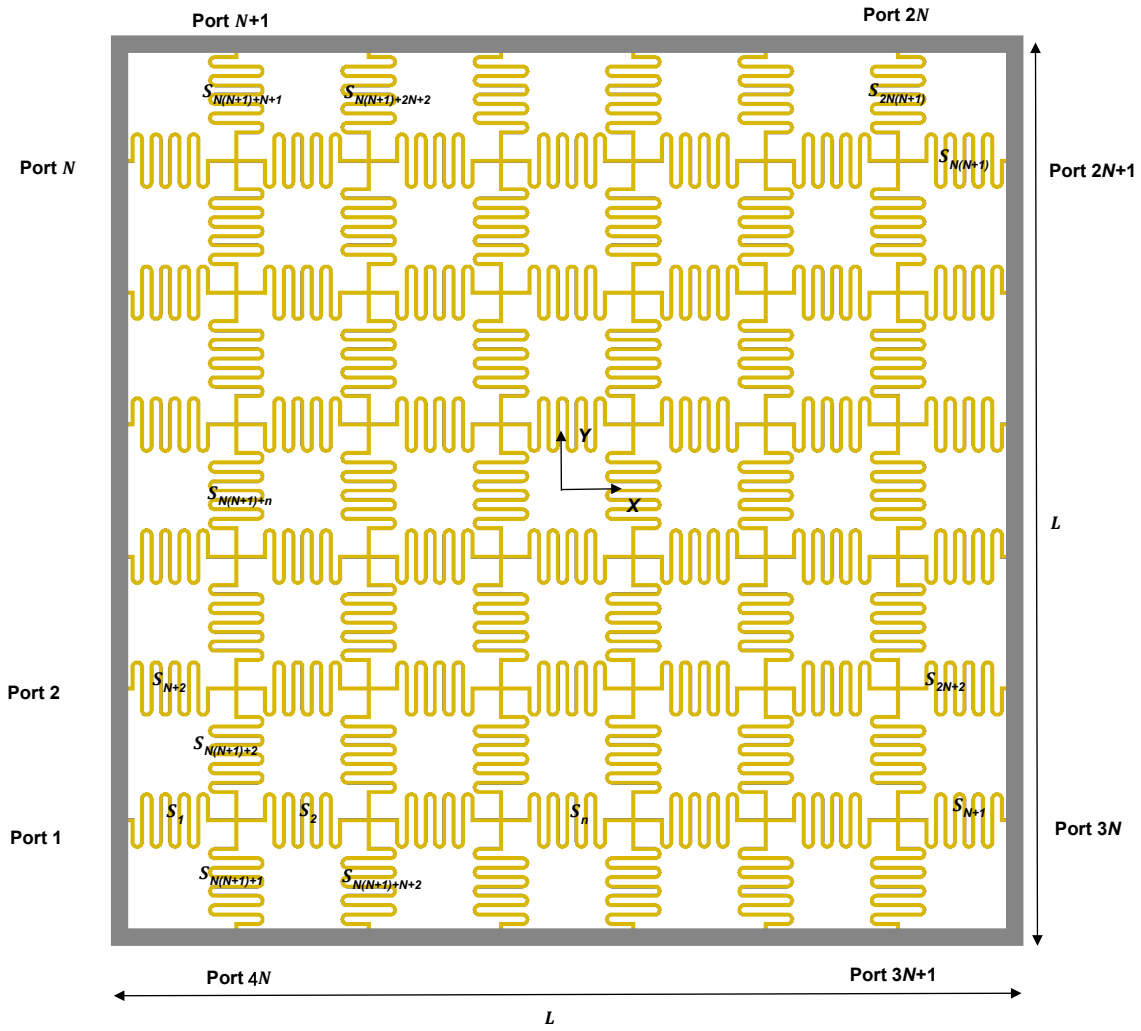

Supplementary Fig. 9 | Schematic illustration of an *N*×*N* structure.

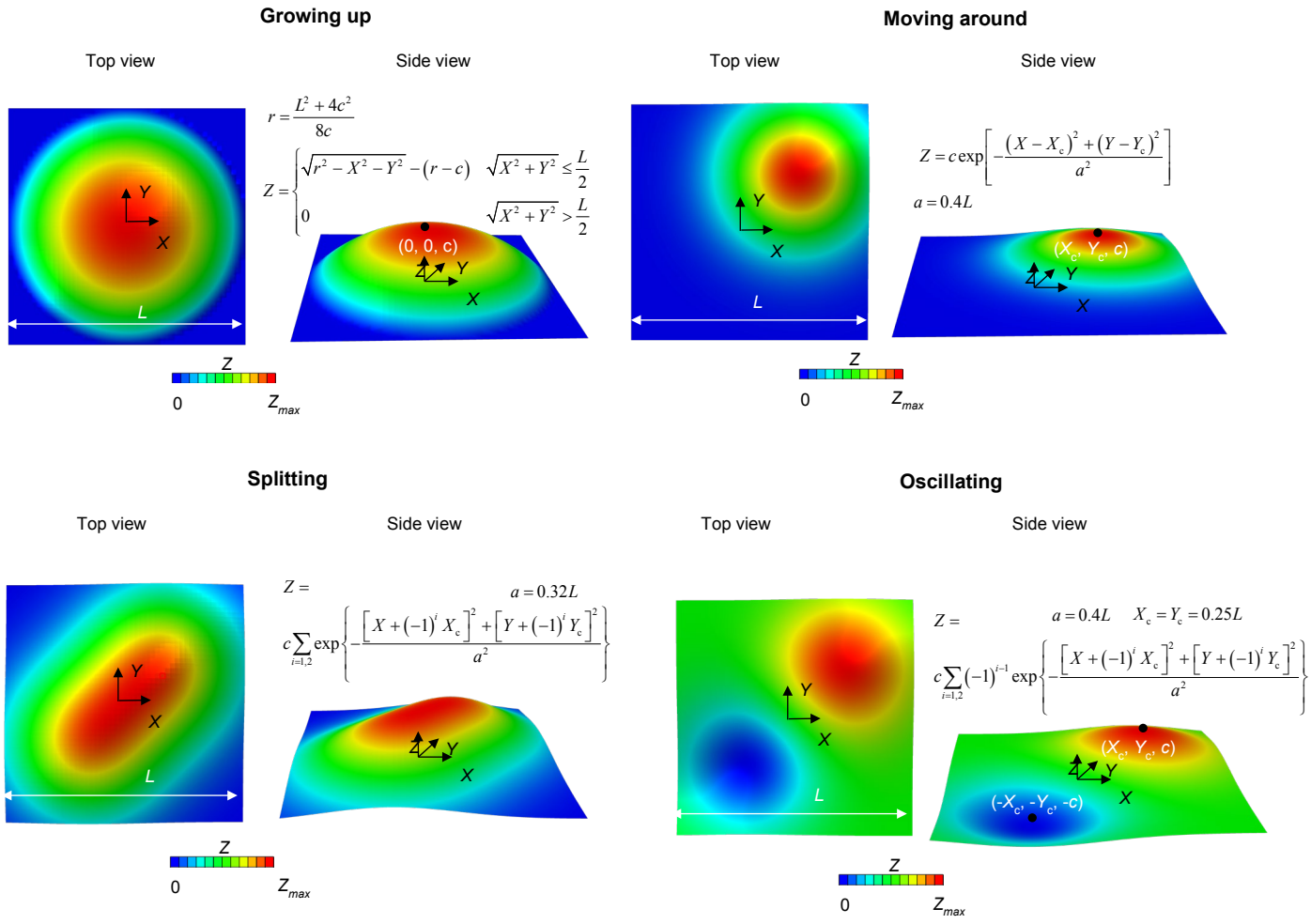

Supplementary Fig. 10 | Schematic illustration and formula of 4 target shape shifting processes.

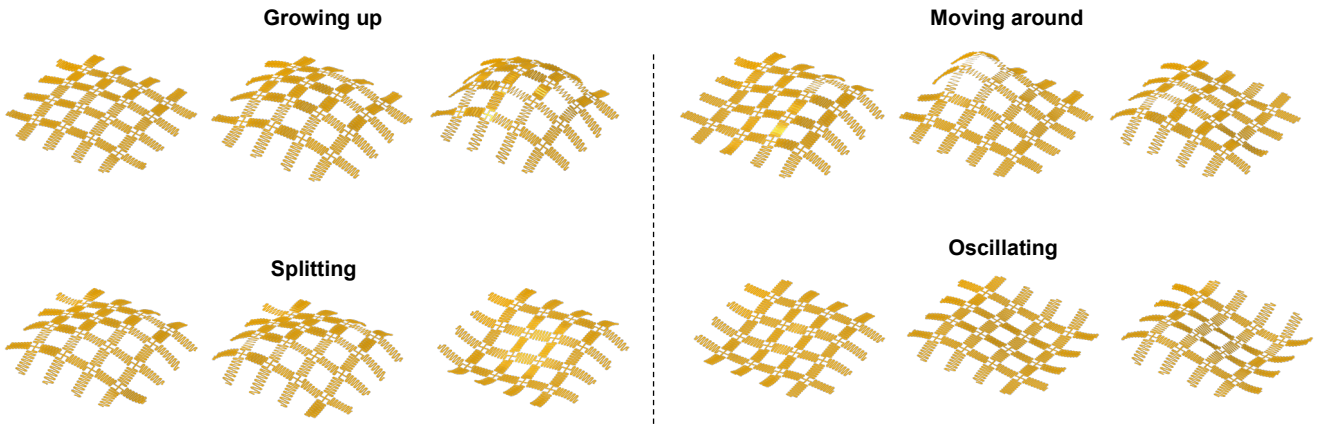

Supplementary Fig. 11 | FEA of the 4×4 sample in Fig. 1d

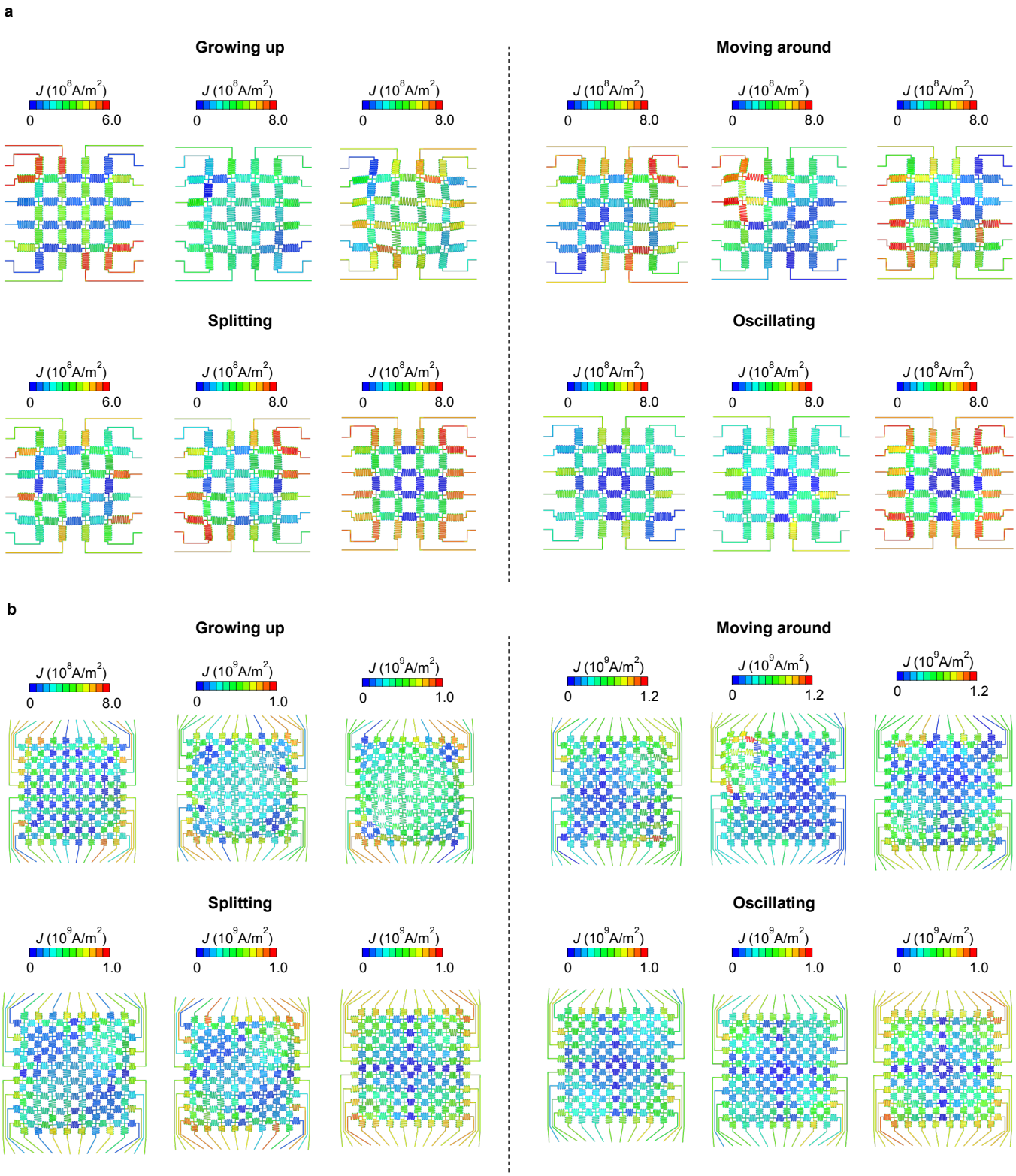

Supplementary Fig. 12 | Distribution of current density for the shapes presented in Fig. 1d. a, 4×4 sample. **b,** 8×8 sample.

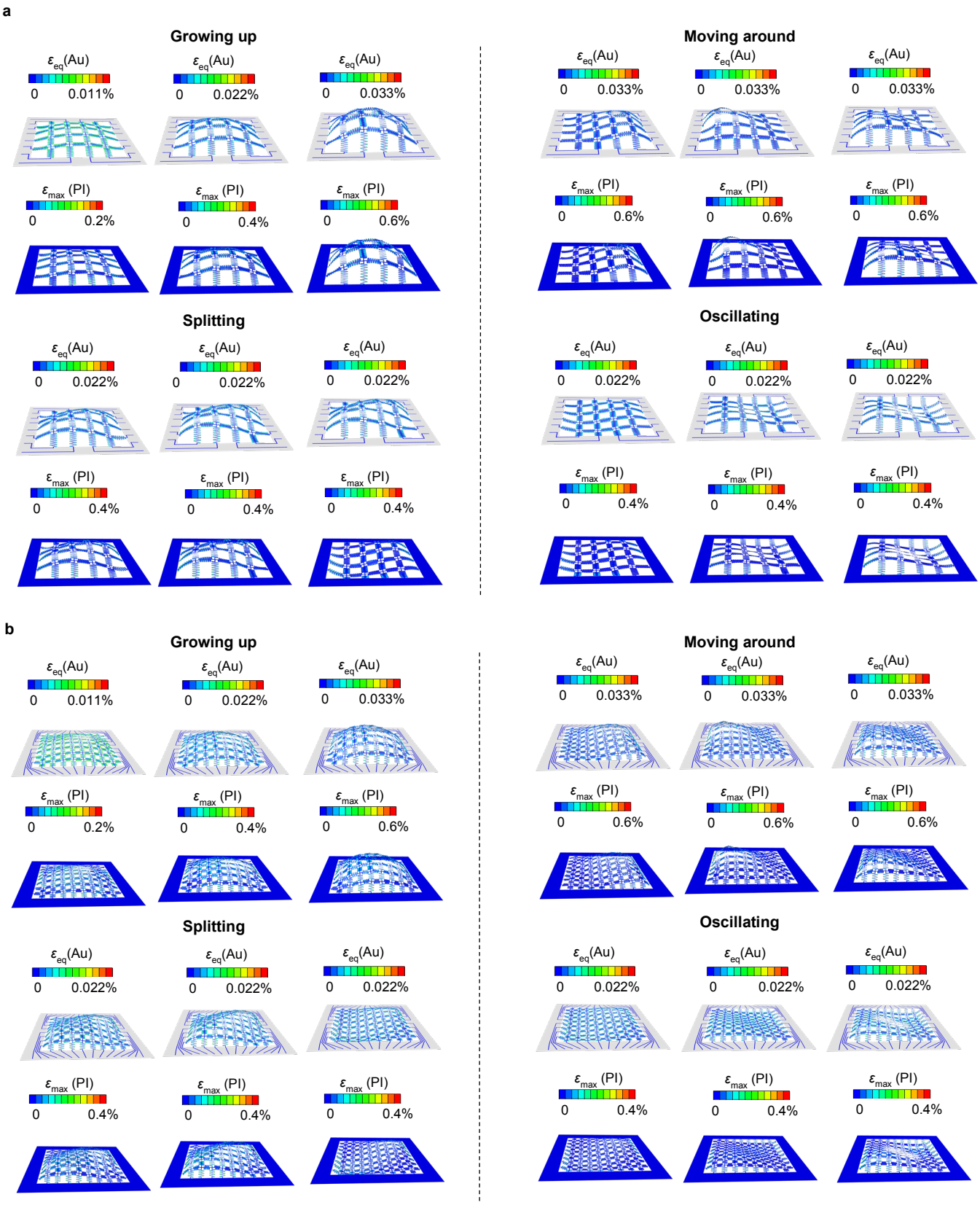

Supplementary Fig. 13 | Distribution of the equivalent strain in Au and the maximum principal strain in PI for the shapes presented in Fig. 1d. a, 4×4 sample. **b,** 8×8 sample.

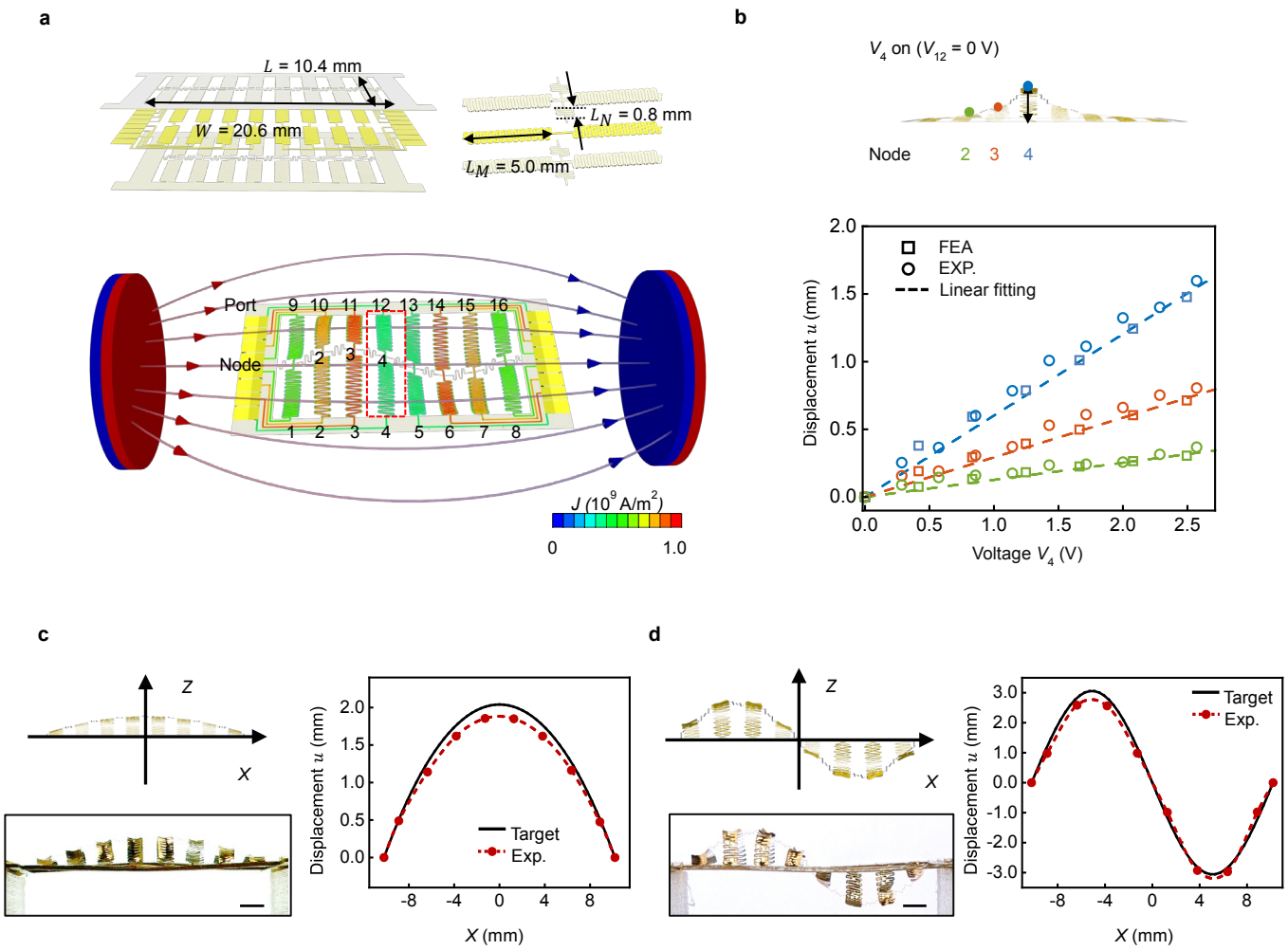

Supplementary Fig. 14 | Modeling and experimental investigations of an array of 8 serpentine beams. a, Schematic illustration of an array of 8 serpentine beams with detailed geometries (L = 10.4 mm, W = 20.6 mm, L_N = 0.8 mm, L_M = 5.0 mm) specified in the exploded views of the sample and a single serpentine unit. **b,** FEA and experimental investigations confirm an approximately linear relationship between representative nodal displacements and portal voltages for the array sample. **c, d,** FEA and experimental results of the array sample (side view) morphing into a spherical shape (c) and sinusoidal shape (d). See Supplementary Note S8 for the target shape functions. Scale bars, 2 mm.

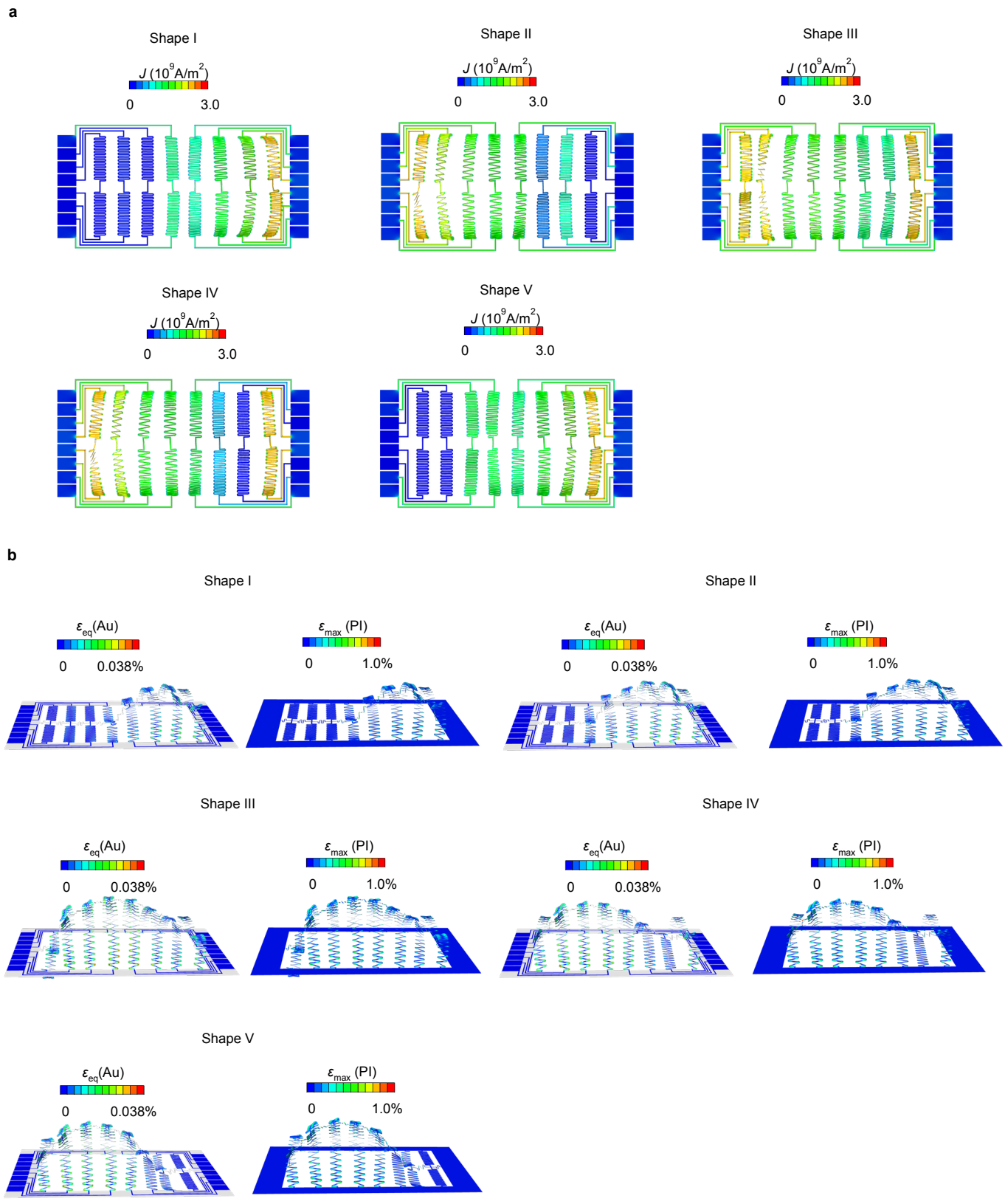

Supplementary Fig. 15 | a, b, Distribution of the current (a), and the equivalent strain in Au and the maximum principal strain in PI (b) for the 5 shapes of the dynamic process presented in Fig. 2a.

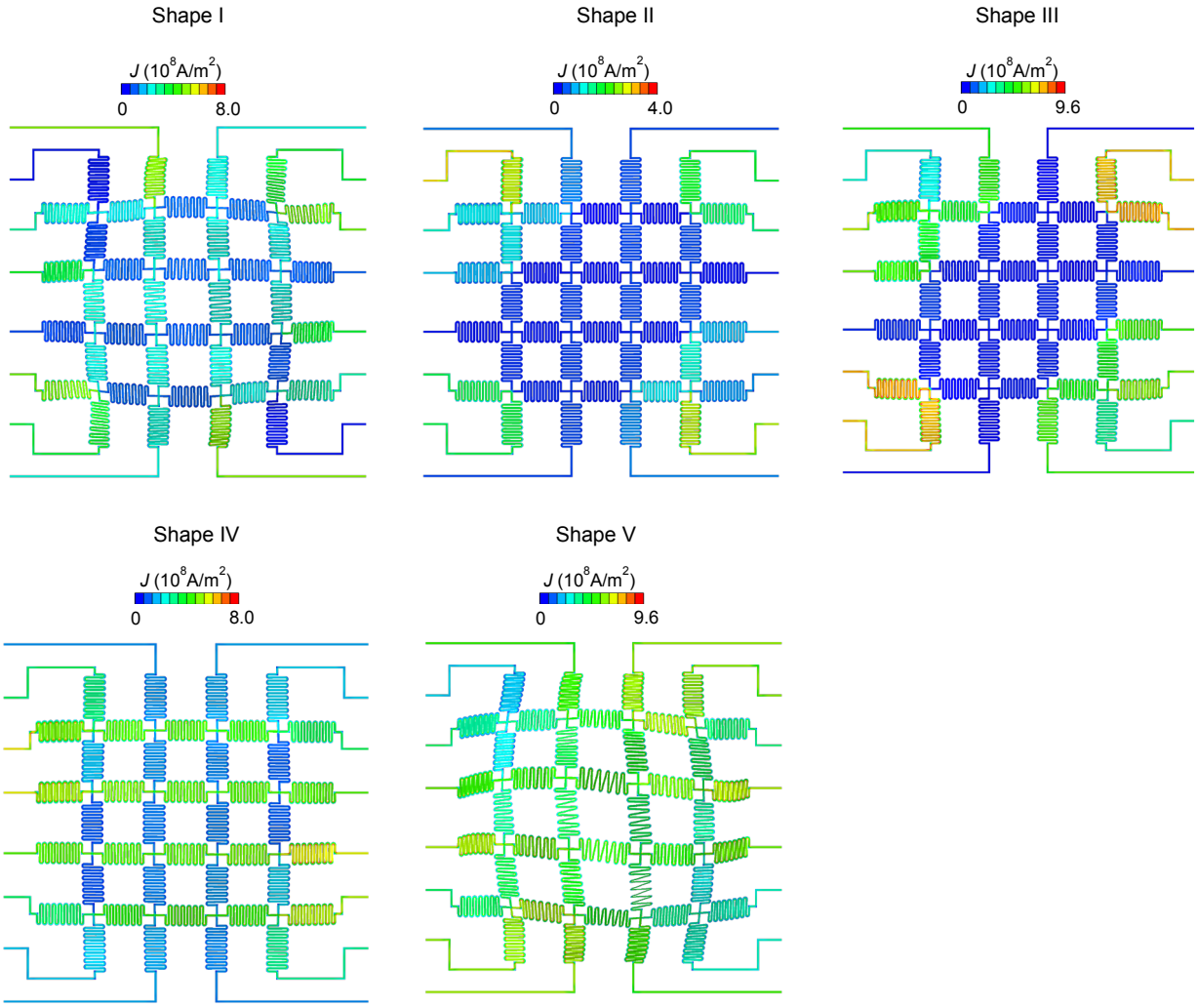

Supplementary Fig. 16 | Distribution of current density for the 5 shapes of the falling droplet imitated by the 4x4 sample in Fig. 2b.

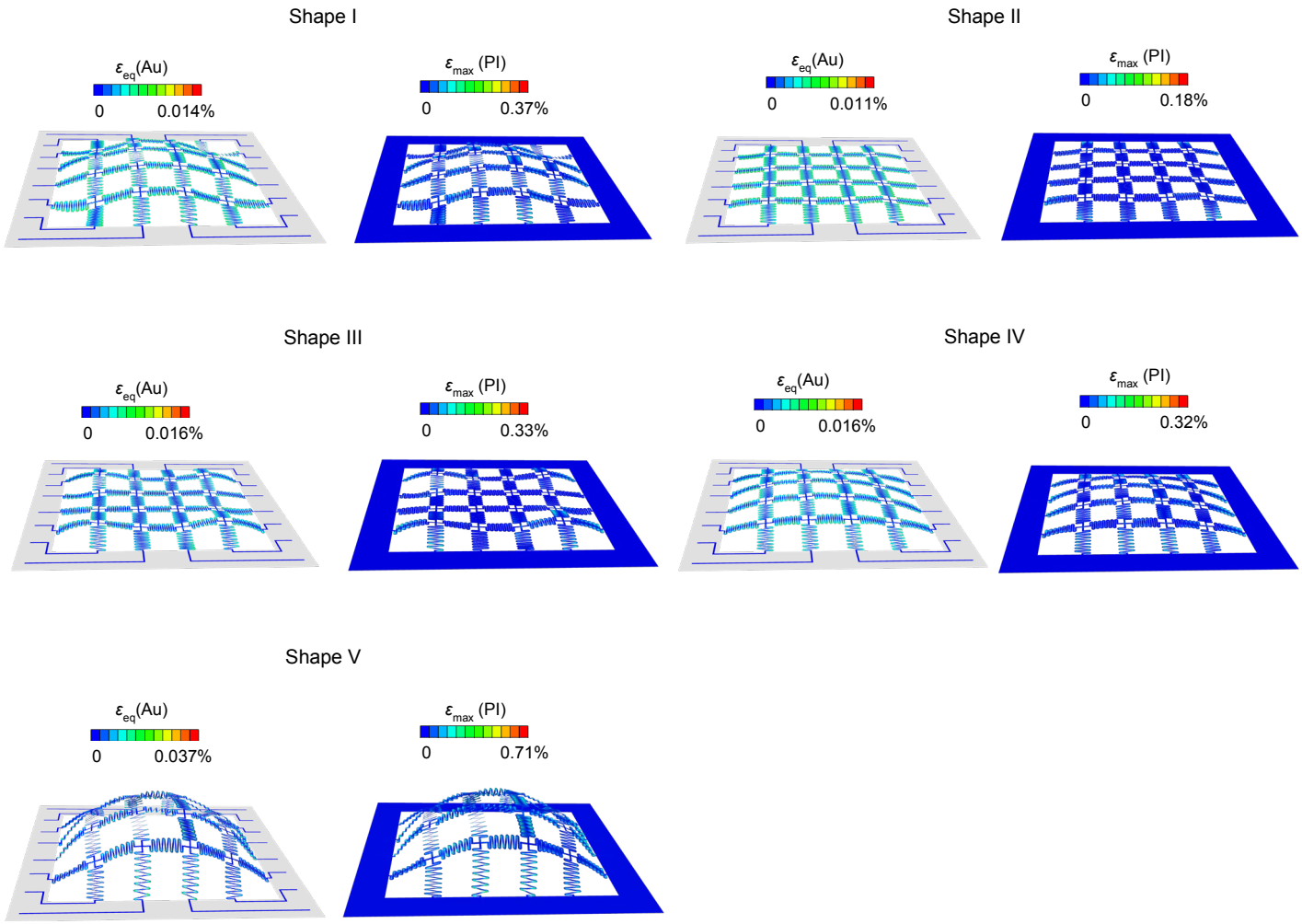

Supplementary Fig. 17 | Distribution of the equivalent strain in Au and the maximum principal strain in PI for the 5 shapes of the falling droplet imitated by the 4x4 sample in Fig. 2b.

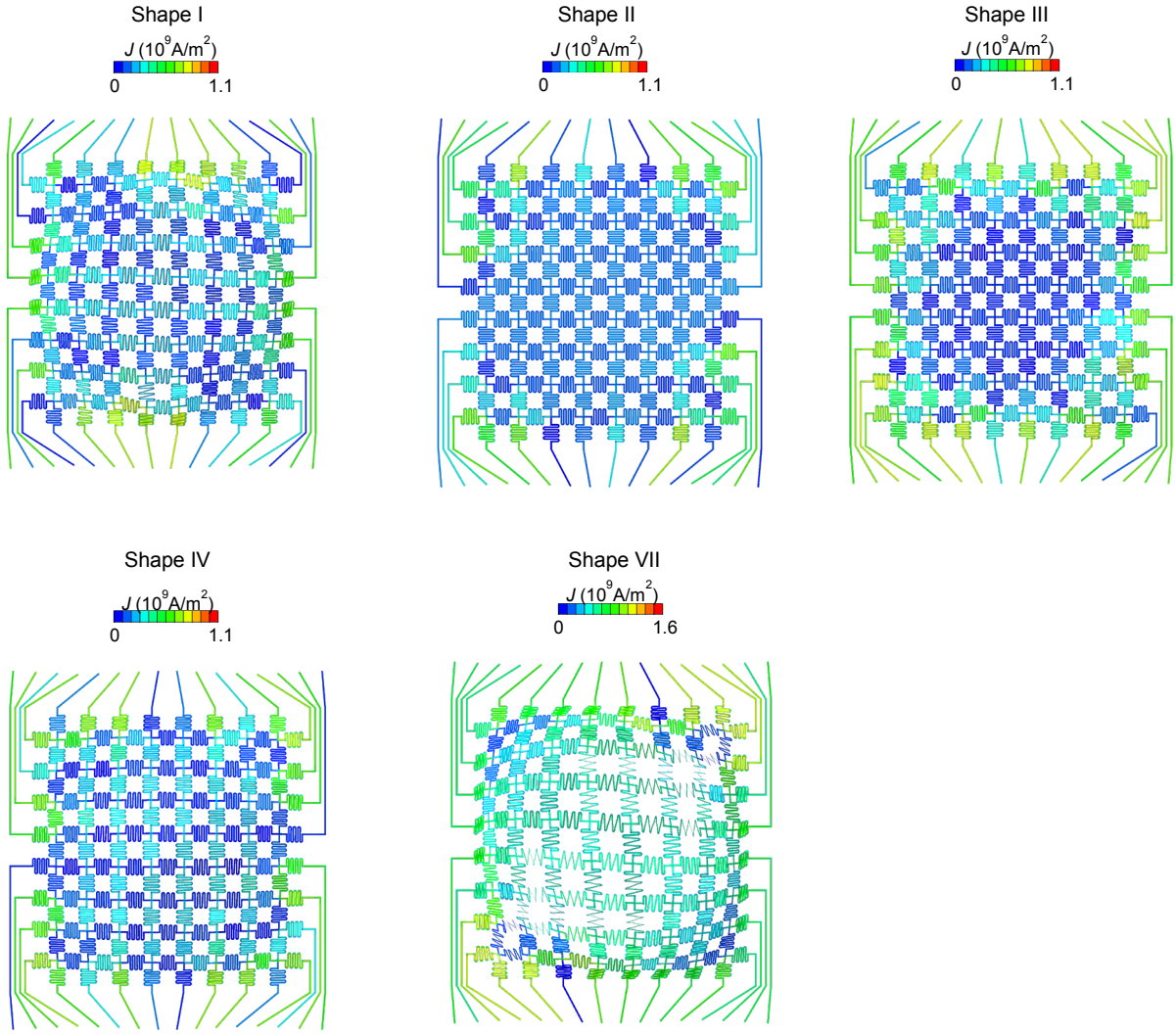

Supplementary Fig. 18 | Distribution of current density for the 5 shapes of the falling droplet imitated by the 8×8 sample in Fig. 2b.

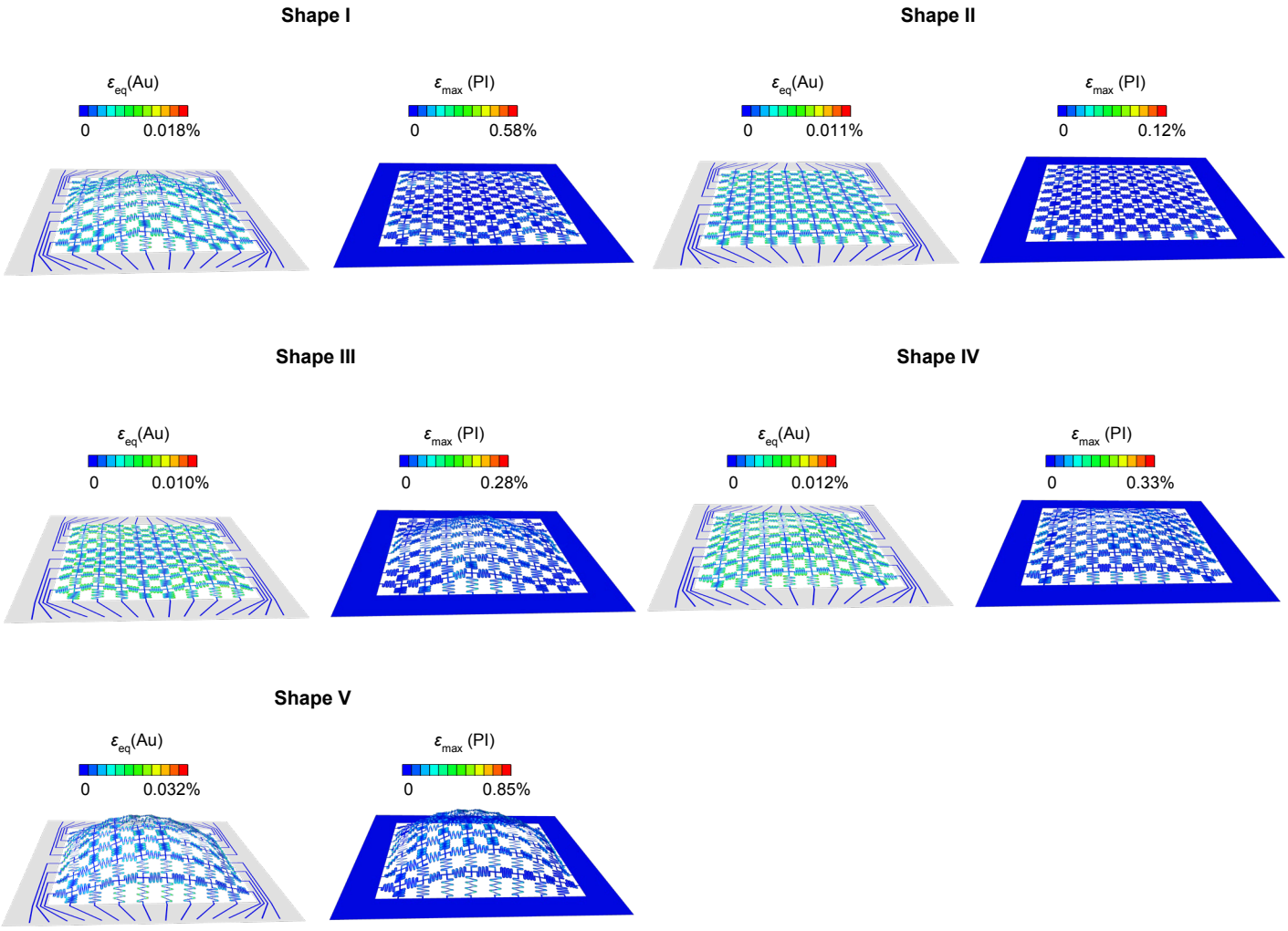

Supplementary Fig. 19 | Distribution of the equivalent strain in Au and the maximum principal strain in PI for the 5 shapes of the falling droplet imitated by the 8×8 sample in Fig. 2b.

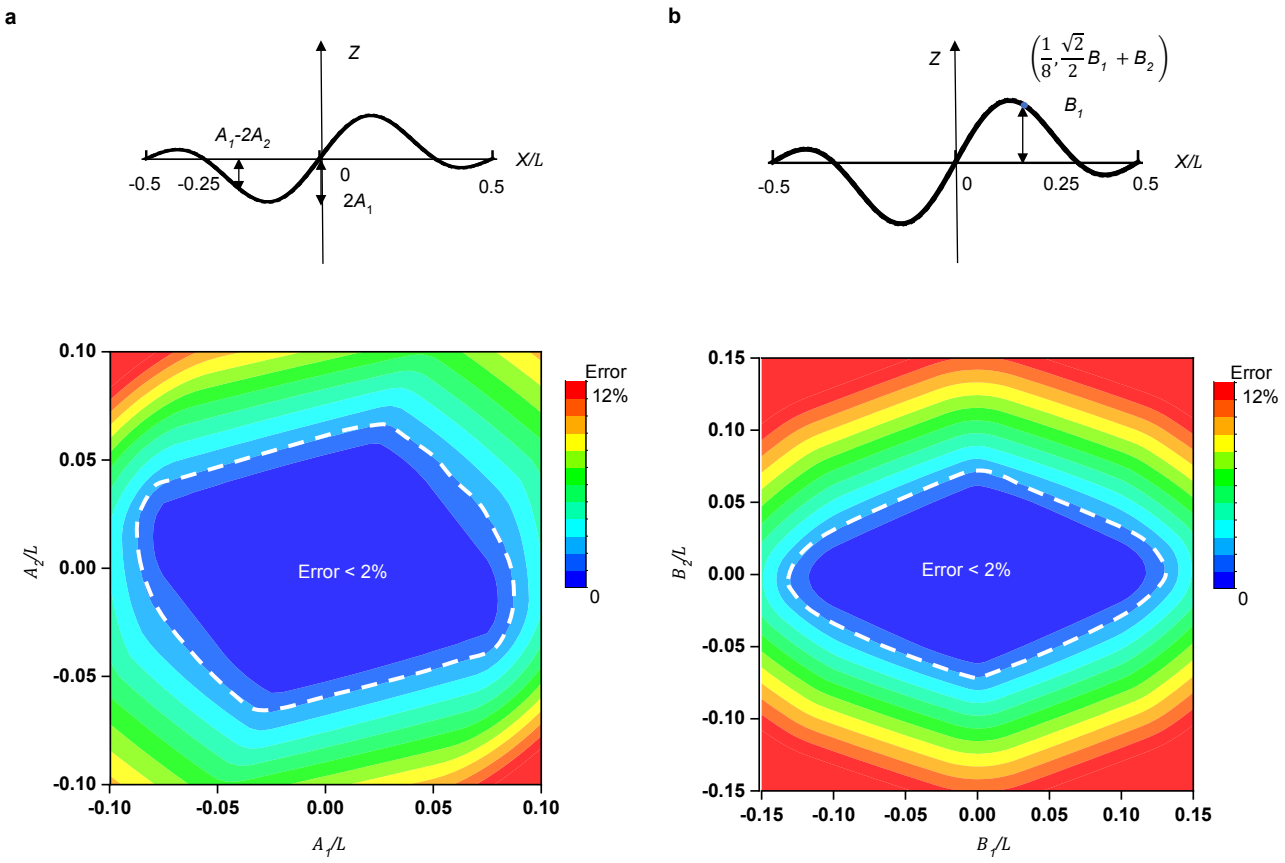

Supplementary Fig. 20 | Error between the deformed an array of 8 serpentine beams and target shapes defined as the Fourier series with the first two terms. a, b, symmetric (a) and asymmetric (b) shapes with respect to the vertical axis at $X = 0$. With parameters in the region enclosed by the white dashed lines, the normalized error is smaller than 2%.

a

$$Z = A_1\left[\cos\left(\frac{2\pi X}{L}\right)+1\right]+A_2\left[\cos\left(\frac{4\pi X}{L}\right)-1\right]+A_3\left[\cos\left(\frac{6\pi X}{L}\right)+1\right]+A_4\left[\cos\left(\frac{8\pi X}{L}\right)-1\right]$$

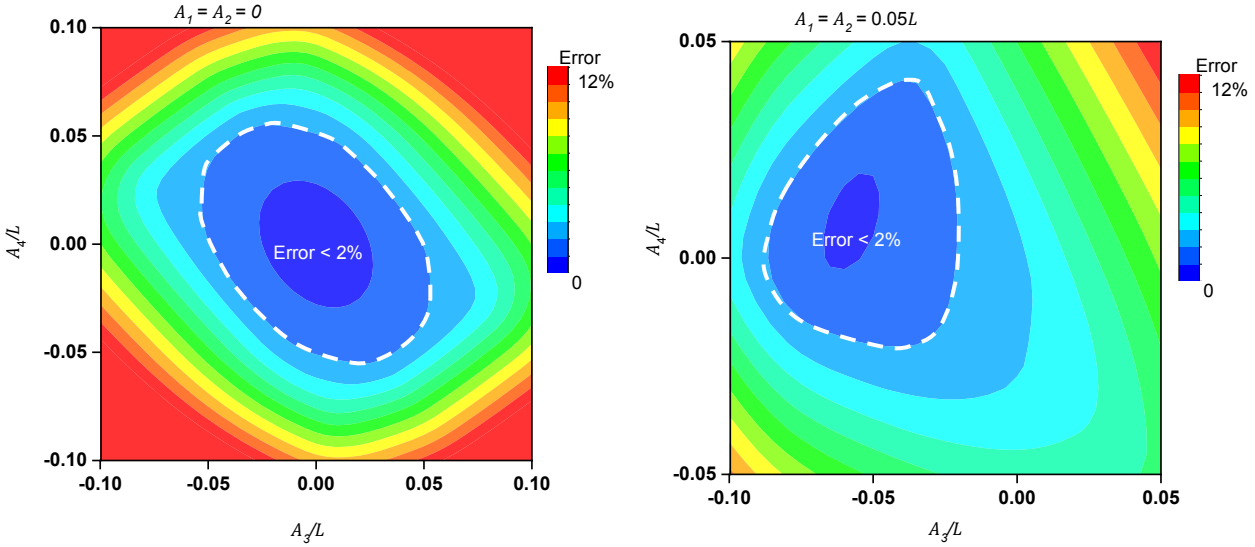

b

$$Z = B_1\sin\left(\frac{2\pi X}{L}\right)+B_2\sin\left(\frac{4\pi X}{L}\right)+B_3\sin\left(\frac{6\pi X}{L}\right)+B_4\sin\left(\frac{8\pi X}{L}\right)$$

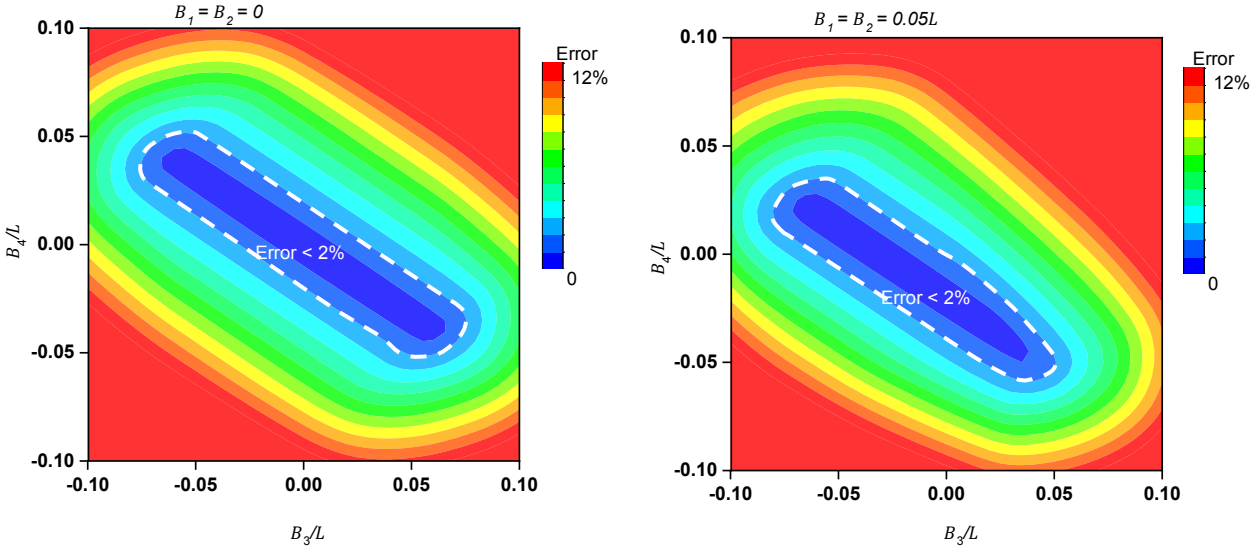

Supplementary Fig. 21 | Error between the deformed an array of 16 serpentine beams and target shapes defined as the Fourier series with the first four terms. a, b, Symmetric (a) and asymmetric (b) shapes with respect to the vertical axis at $X = 0$. With parameters in the region enclosed by the white dashed lines, the normalized error is smaller than 2%.

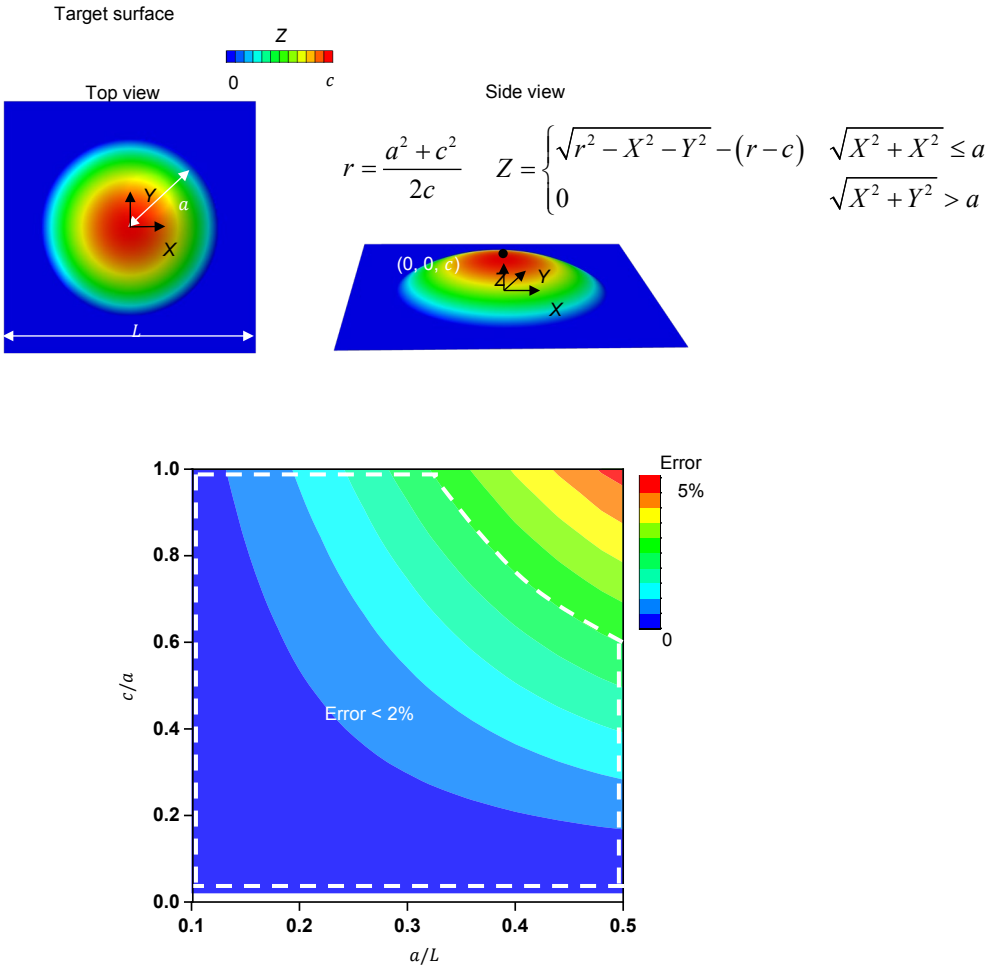

Supplementary Fig. 22 | Error between the deformed 4×4 sample and target shapes defined by a spherical cap. With parameters in the region enclosed by the white dashed lines, the normalized error is smaller than 2%.

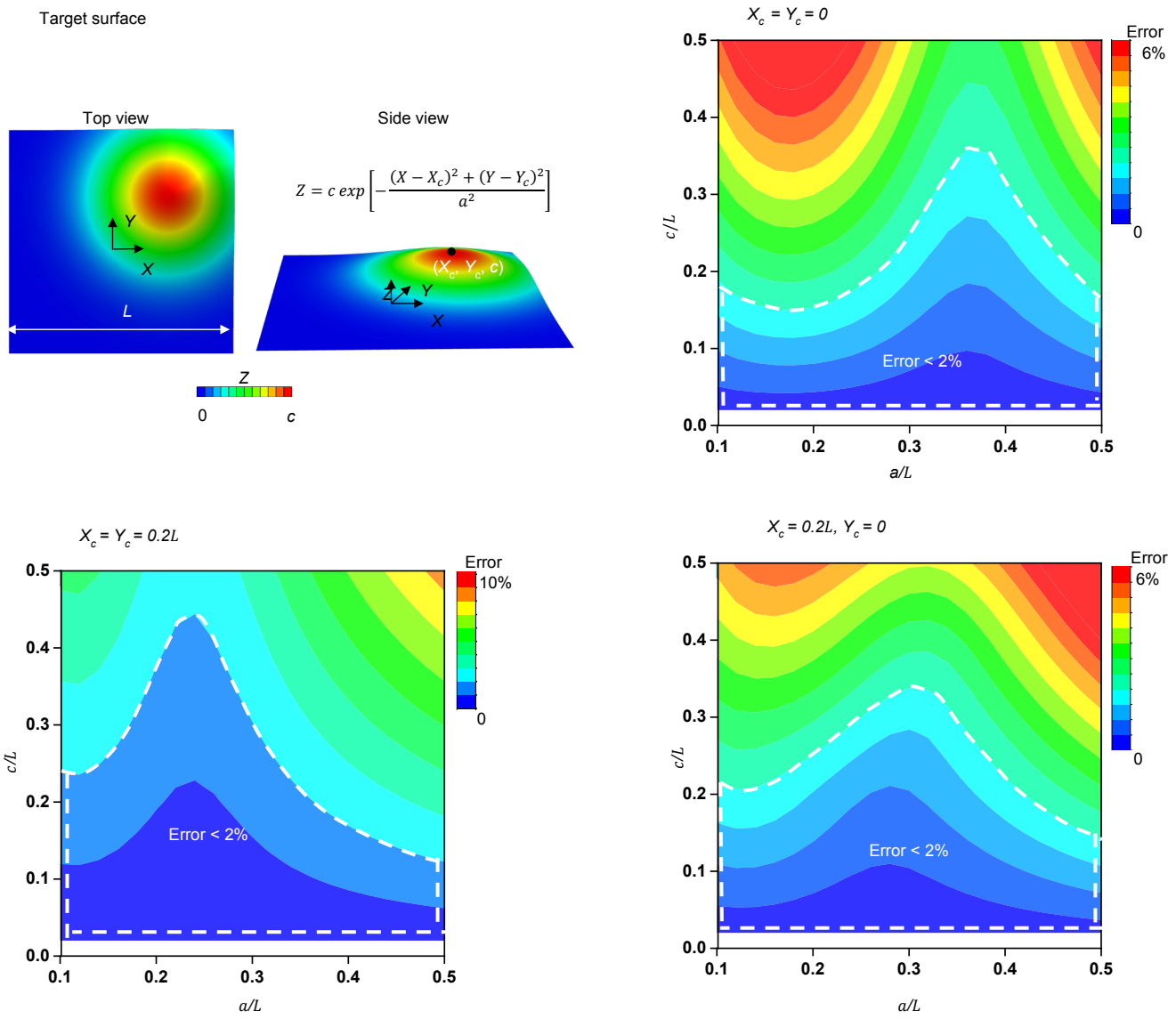

Supplementary Fig. 23 | Error between the deformed 4×4 sample and target shapes defined by a Gaussian function. With parameters in the region enclosed by the white dashed lines, the normalized error is smaller than 2%.

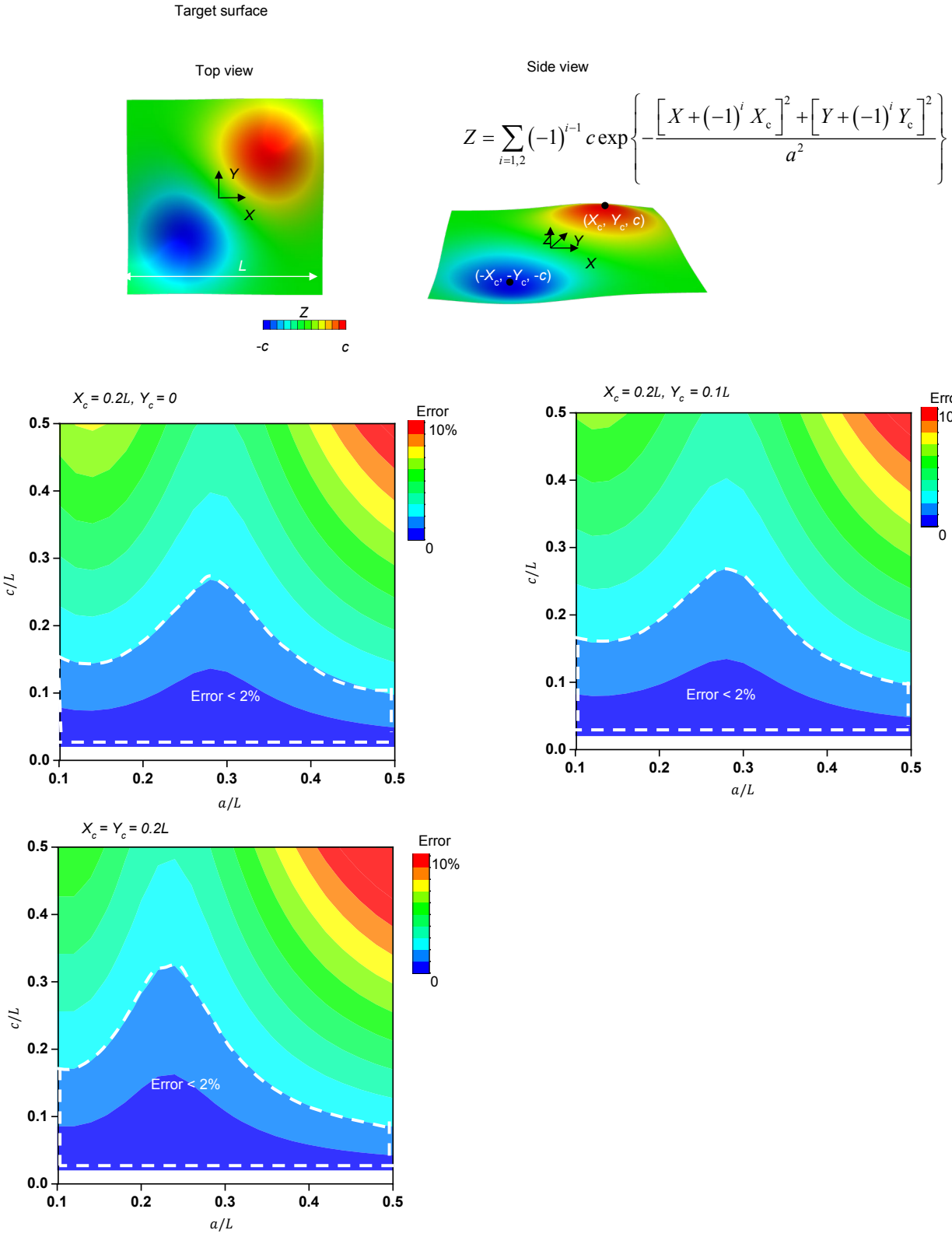

Supplementary Fig. 24 | Error between the deformed 4×4 sample and target shapes defined by a Gaussian function with two terms. With parameters in the region enclosed by the white dashed lines, the normalized error is smaller than 2%.

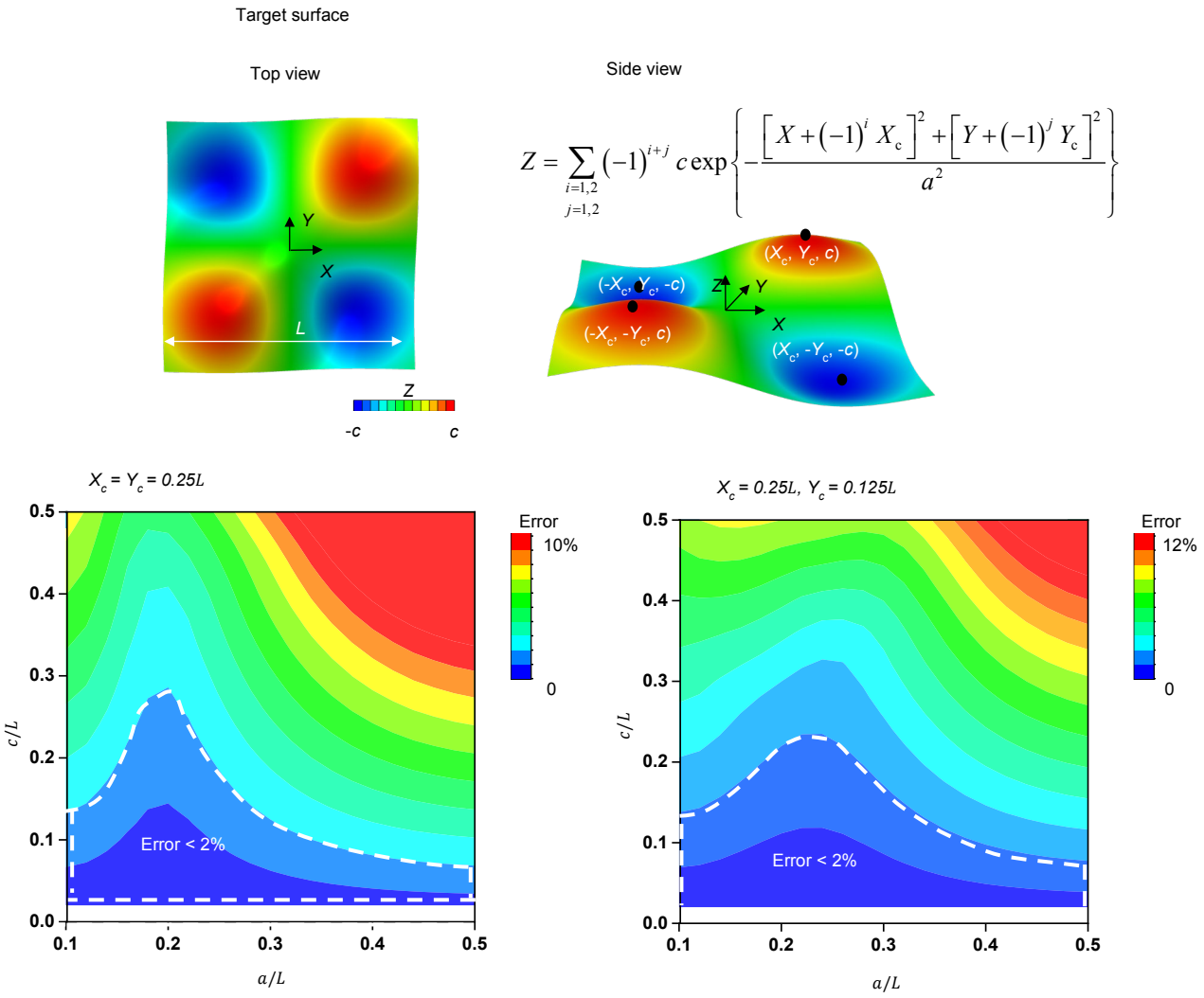

Supplementary Fig. 25 | Error between the deformed 4×4 sample and target shapes defined by a Gaussian function with four terms. With parameters in the region enclosed by the white dashed lines, the normalized error is smaller than 2%.

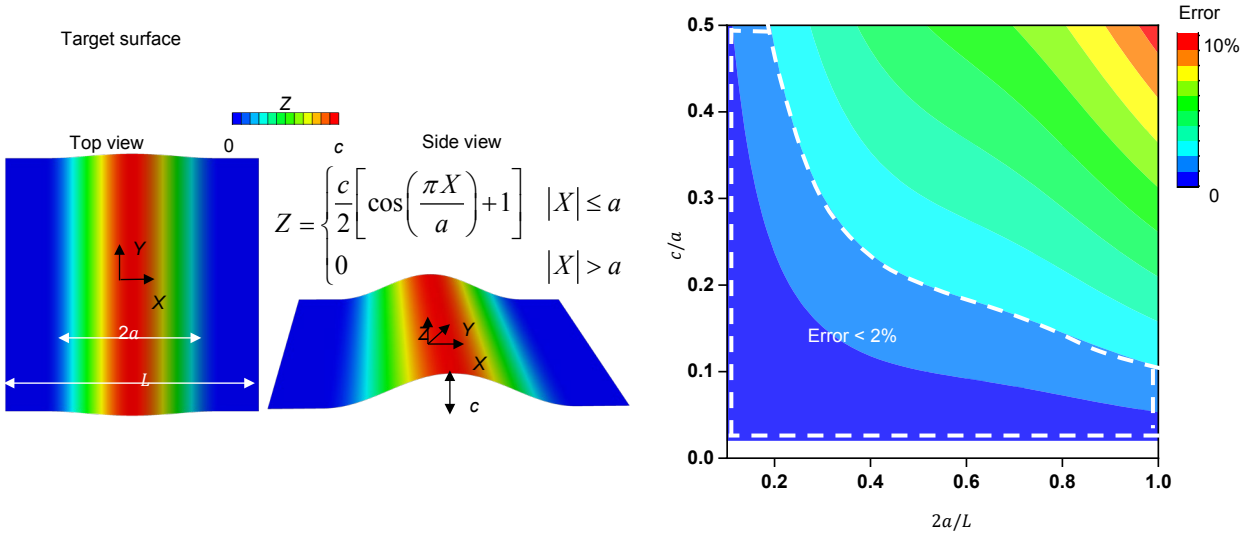

Supplementary Fig. 26 | Error between the deformed 4×4 sample and target shapes defined by a sinusoidal function. With parameters in the region enclosed by the white dashed lines, the normalized error is smaller than 2%.

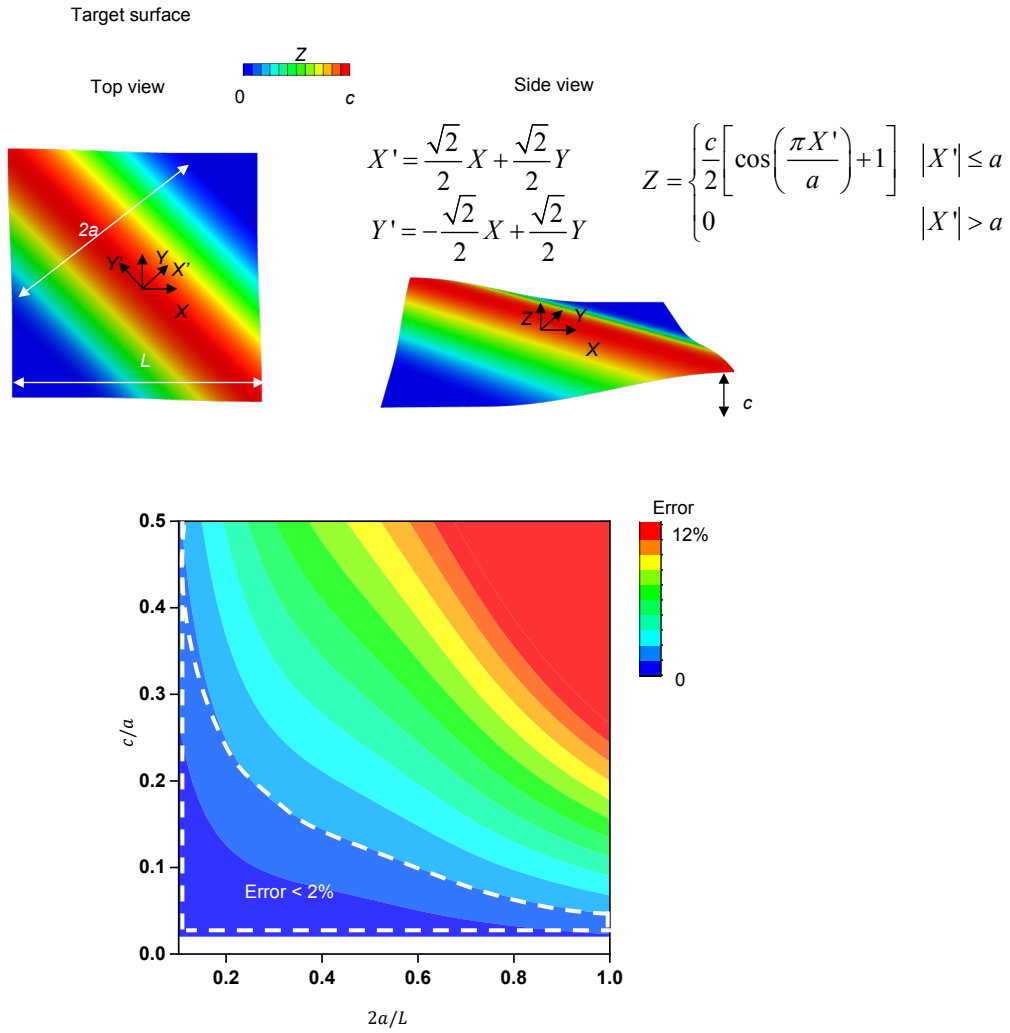

Supplementary Fig. 27 | Error between the deformed 4×4 sample and target shapes defined by a sinusoidal function along the diagonal direction. With parameters in the region enclosed by the white dashed lines, the normalized error is smaller than 2%.

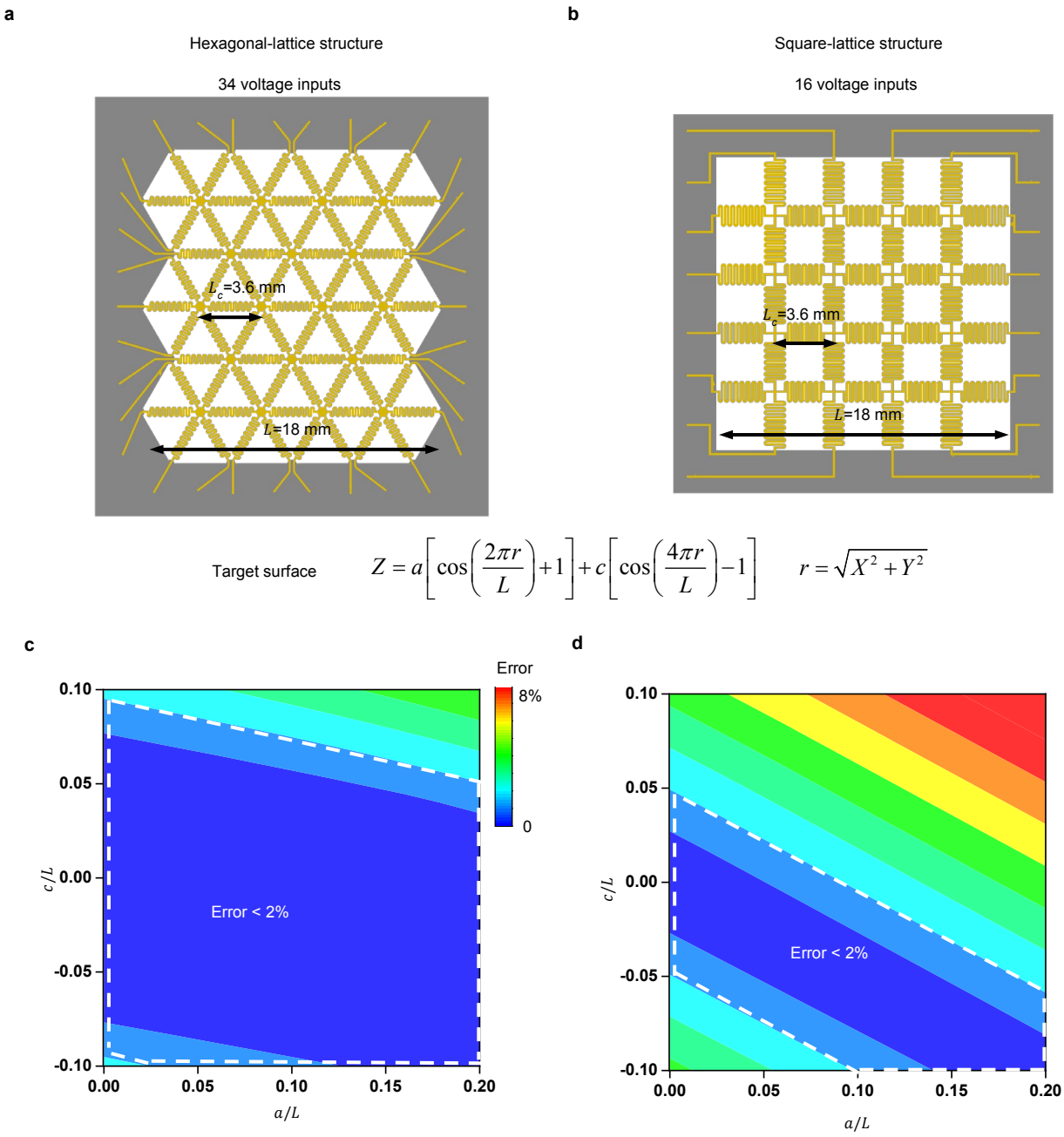

Supplementary Fig. 28 | A hexagonal-lattice structure to increase the number of voltage inputs. a, Schematic illustration of a hexagonal-lattice structure with 34 voltage-input ports, in comparison with **b,** a square-lattice structure of approximately the same overall and unit-cell sizes, L and L_c. **c,** Error map of the hexagonal structure morphing into a subset of target shapes. A cap of 2% error defines the accessible range of producible shapes. **d,** Error map of the square-lattice structure targeting the same subspace as in (b).

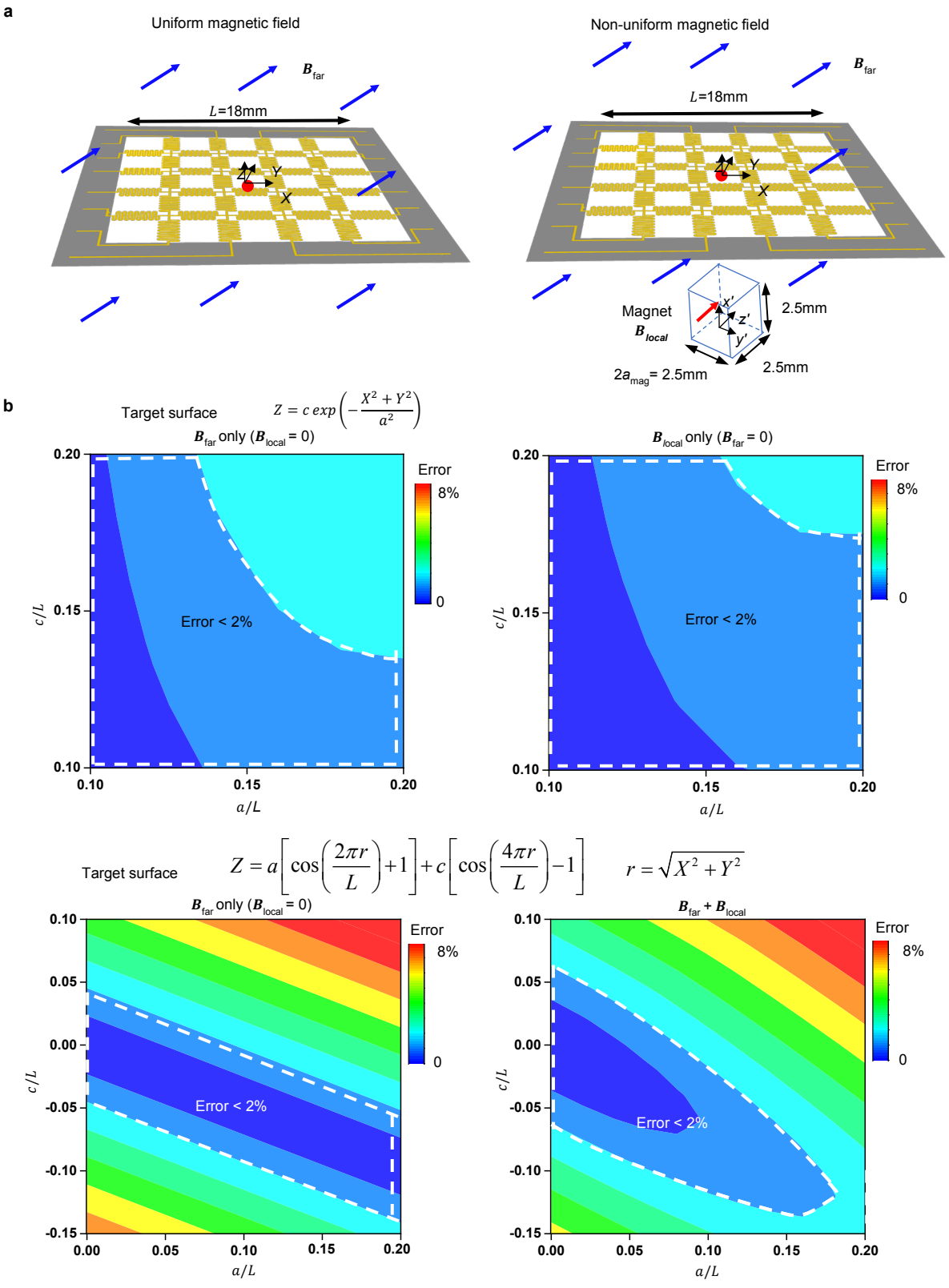

Supplementary Fig. 29 | FEA investigation of a 4×4 sample morphing into example targeting subspaces in uniform and non-uniform magnetic fields. a, Schematic illustration of a 4×4 mesh structure in a uniform magnetic field $\boldsymbol{B}_{far}$ (magnitude 224 mT) and a non-uniform magnetic field $\boldsymbol{B}_{far}$ + $\boldsymbol{B}_{local}$, where $\boldsymbol{B}_{local}$ is generated by a small magnet (magnetization M = 1.1×10^6 A/m, see Supplementary Note S2.1) 2 mm below the center of the structure. **b and c,** Numerical results of the error between the deformed structure target shapes. In the left panels of b and c, $\boldsymbol{B}_{local}$ is set to be zero such that the magnetic field is uniform. In the right panel of b, $\boldsymbol{B}_{far}$ is set to be zero such that the magnetic field is localized around the center.

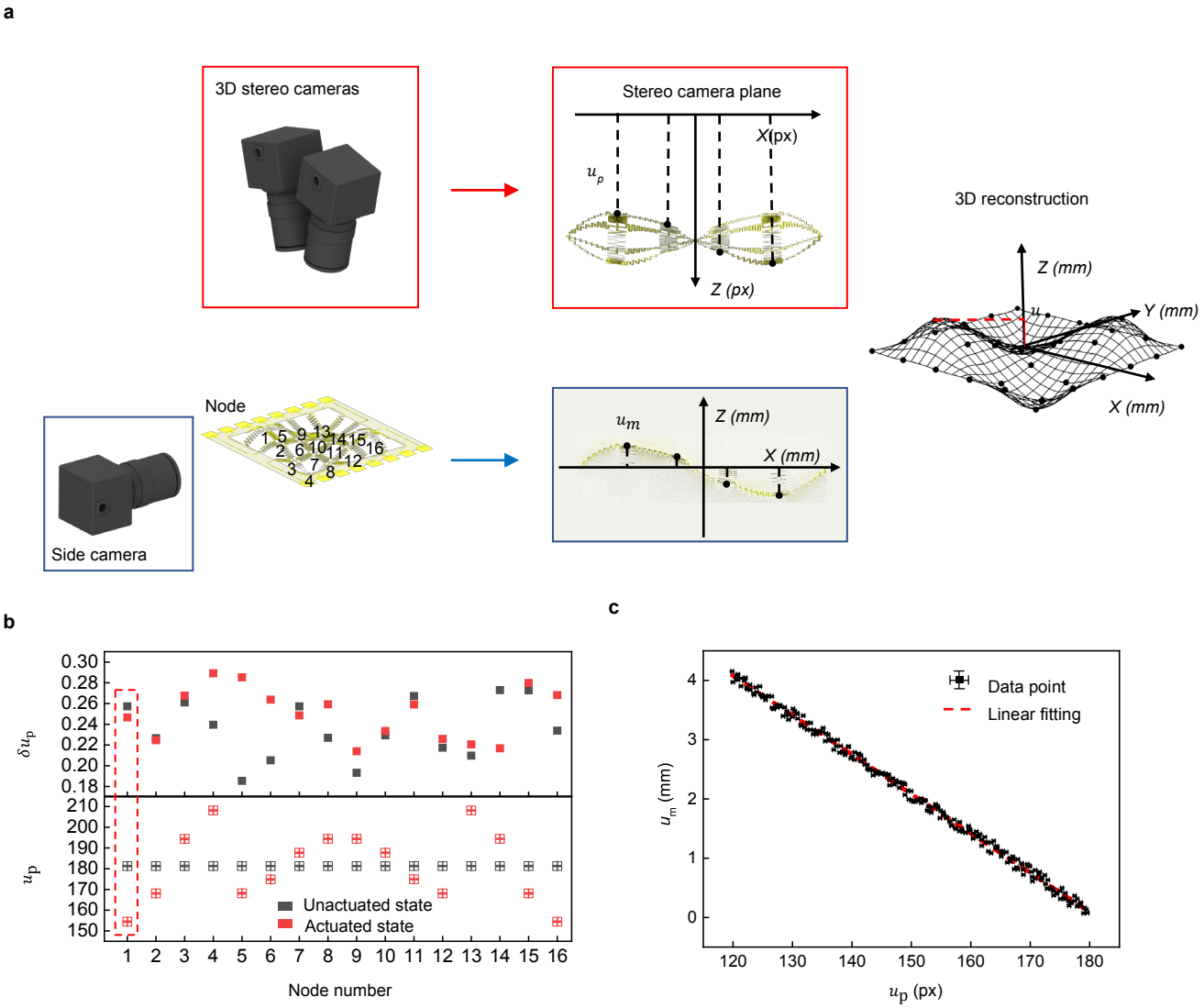

Supplementary Fig. 30 | Characterization of the resolution and uncertainty of 3D imaging. a, The illustration of the characterization experiment. A side camera (Webcams, ELP, 3840 x 2160-pixel resolution, 30 fps) provides the measurement of nodal displacement (u_m) as the ground truth for 3D imaging calibration. Two cameras (Webcams, ELP, 3840x2160-pixel resolution, 30 fps) are placed symmetrically above the sample. Stereo-imaging method provides a measurement of depth (u_p) of each node below the camera plane in a unit of pixels (px). **b,** The depths (u_p) of the 16 nodes of a 4×4 sample under a cyclic actuation (200 cycles of shape IV in Extended Data Fig. 5a) are monitored by the stereo-imaging method. The measured depth (u_p) in either actuated or unactuated state follows a Gaussian distribution. Analysis of the distribution of u_p reveals a mean standard deviation of 0.25 px. **c,** Applying Deming regression on u_m vs. u_p provides a linear model for the 3D reconstruction, $u(u_\mathrm{p})$.

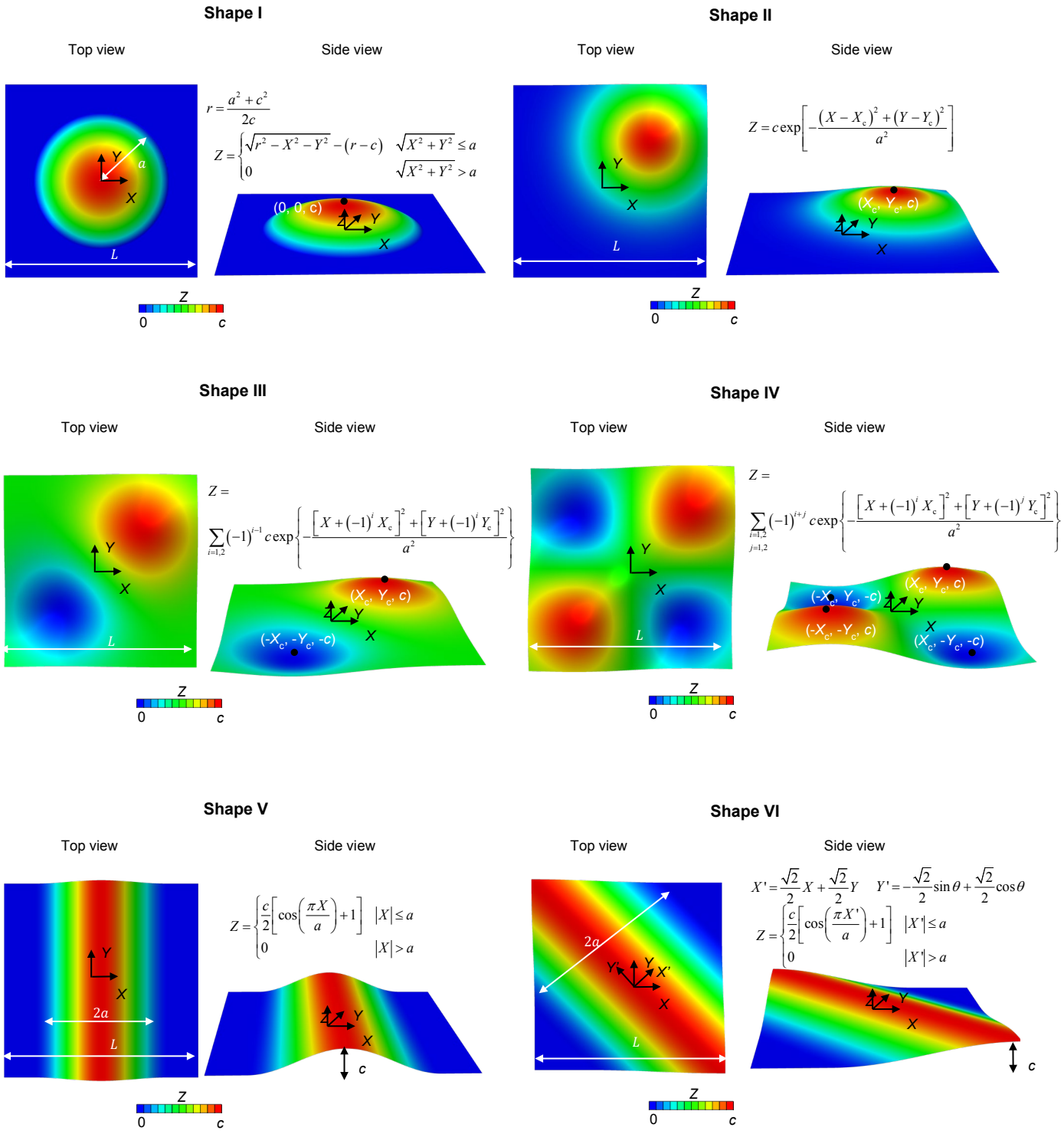

Supplementary Fig. 31 | Schematic illustration and formula of 6 classes of target shapes.

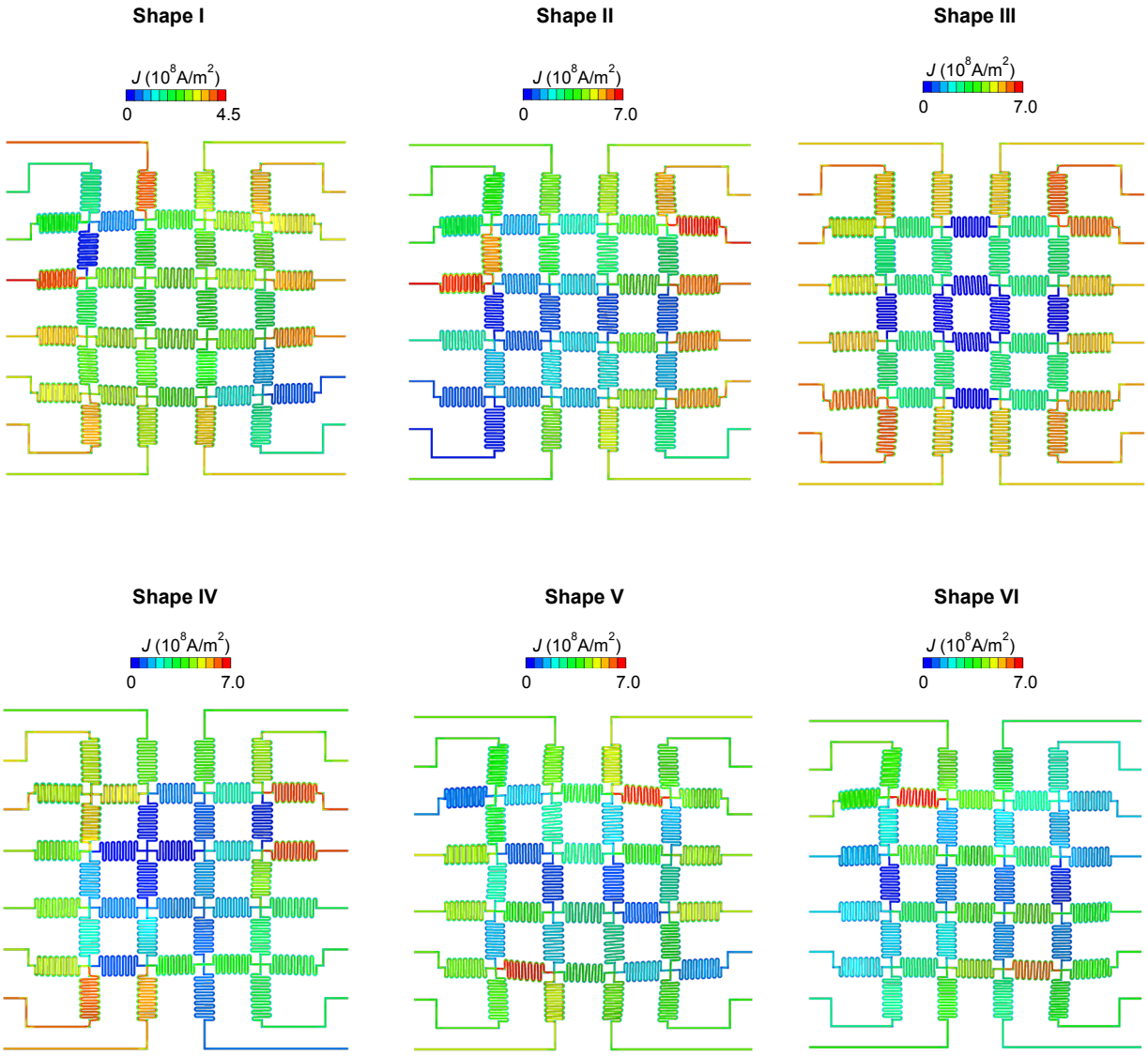

Supplementary Fig. 32 | Distribution of current density for the 6 target shapes presented in Extended data Fig. 5a.

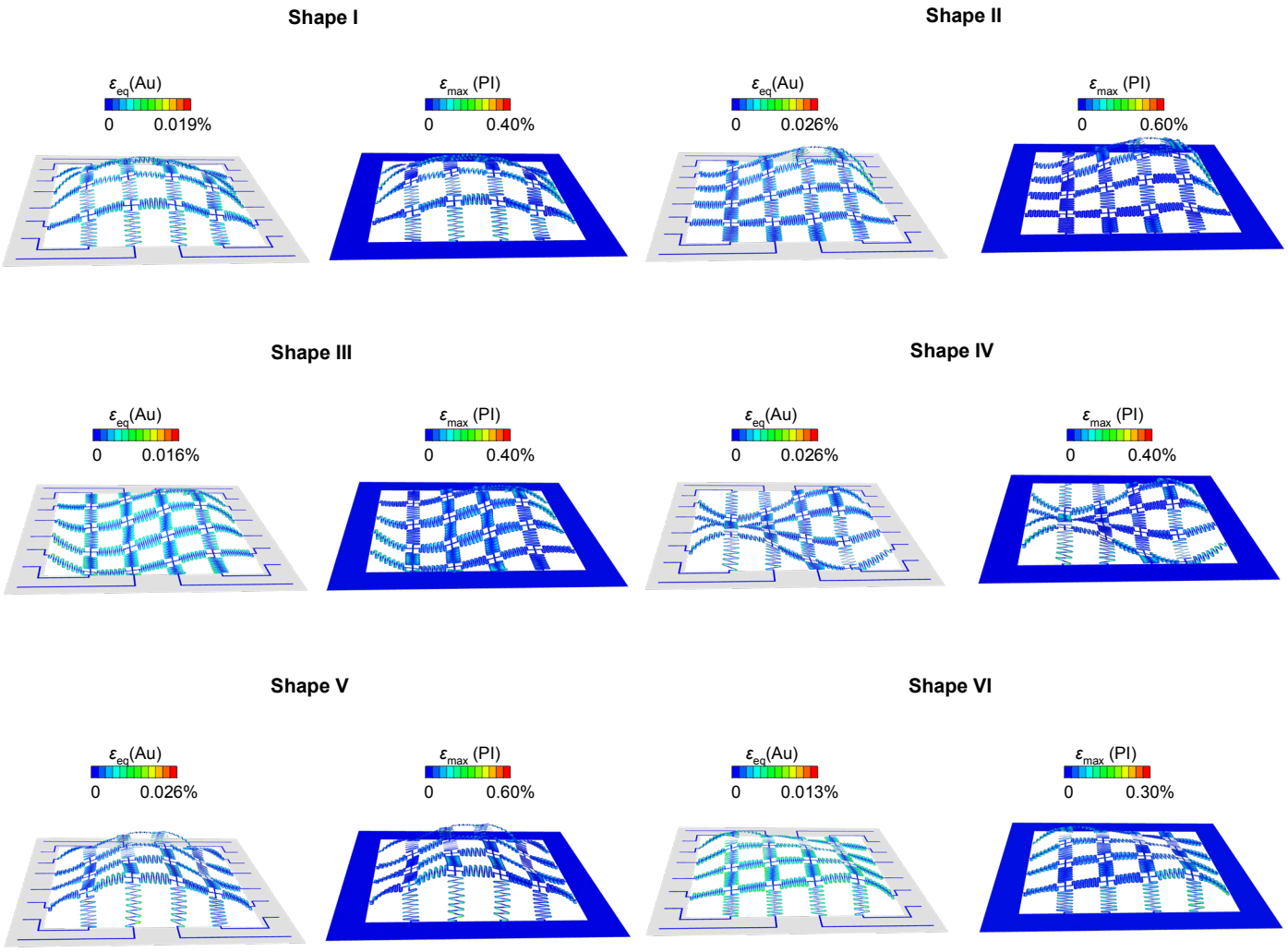

Supplementary Fig. 33 | Distribution of the equivalent strain in Au and the maximum principal strain in PI for the 6 abstract shapes presented in Extended data Fig. 5a.

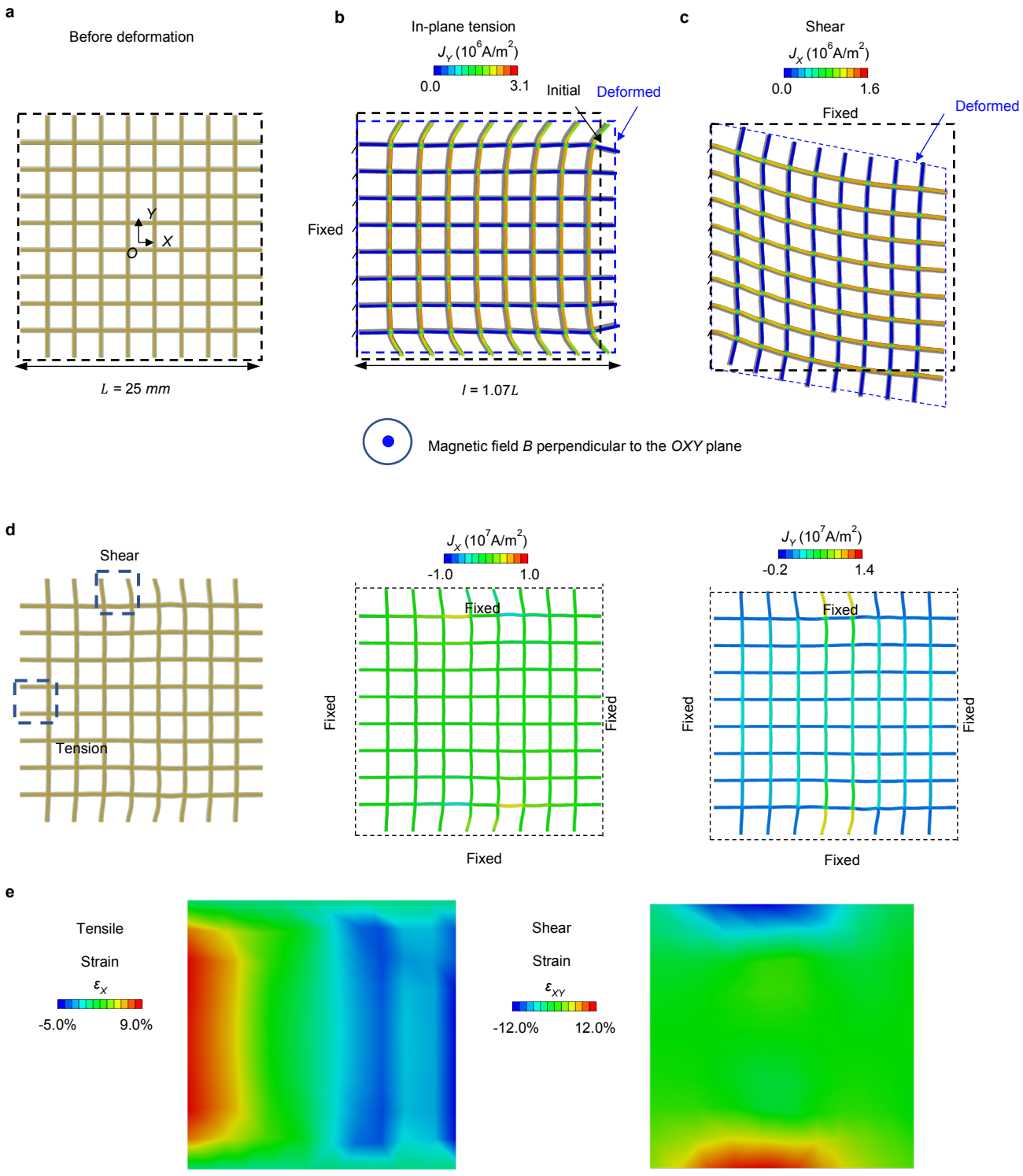

Supplementary Fig. 34 | Illustration of appreciable in-plane deformations. a, Schematic illustration of a mesh structure with sufficiently small in-plane stiffness (~0.02 N). **b,** FEA result of an in-plane tension deformation of a one-end fixed sample, with the *Y*-component of the current density (J_Y) overlaid (*X*-component J_X ~ 0). Applying uniform electric current (0.5 A) in the *Y*-direction and a uniform magnetic field (*B* = 200 mT) perpendicular to the *OXY* plane induces Lorentz forces on the mesh in the *X*-direction. **c,** FEA result of the shear deformation of a one-end fixed sample induced by a uniform electric current (0.25 A) in the *X*-direction. **d,** Complex spatial varying in-plane deformations of an all-side fixed sample (left) achieved by a non-uniform electric current distribution (middle and right). **e,** contour map of the strain in (d), constructed from the nodal displacements.

Update Actuation	Wait for Steady State	3D imaging			Optimization	Sum
		Stereo Imaging	Template Matching	Projection and Reconstruction		
0.06±0.01 s	0.1±0.05 s	0.08±0.04 s	0.11±0.05 s	0.00±0.00 s	0.00±0.00 s	0.35±0.15 s

Supplementary Table 1 | Function evaluation time budget. Experimentally measured time expenditure of each step to complete one function evaluation for the experiment-driven optimization of a 4×4 sample is presented. Each function evaluation costs an average of 0.35 s.

Supplementary Video legends

Supplementary Video 1. A 4×4 and an 8×8 sample morphing into a dynamic shape-shifting process.

A 4×4 and an 8×8 sample morphs into four target shape-shifting processes with uniform velocities and constant frequency: growing up, moving around, splitting, and oscillating. A 4×4 sample morphs into the same processes with control on instantaneous velocity and acceleration of the dynamics. The actuation voltages (designed via model-driven approach) are updated at a rate of 10 fps.

Supplementary Video 2. A 4×4 sample morphing into the dynamic process of a droplet hitting a solid surface.

A 4×4 sample morphs into a bouncing water droplet captured in slow motion by a high-speed camera (10,000 fps). The dynamic shape-shifting process consists of five stages: falling onto the surface, spreading out, bouncing back, vibrating and stabilizing. The 3D shapes of the droplet extracted from the video frames are normalized by the sample size. The actuation voltages (designed via model-driven approach) are updated at a rate of 10 fps.

Supplementary Video 3. A 4×4 sample morphing into target abstract shapes via the experiment-driven process.

A 4×4 sample starts from a zero-actuation state and self-evolves into target explicit shapes (Shape I, III, IV in Extended Data Fig. 5a). An optical camera captures the evolving sample during the experiment-driven process. The in-time 3D-reconstructed surface and the evaluation of the loss function $f(\mathbf{V} = \mathbf{0})$ over the number of function evaluations are synced with the video with a 10× playback speed. In all cases, the loss function f $(\mathbf{V} = \mathbf{0})$ reaches a value below $0.005f(\mathbf{V} = 0)$ (stopping criterion) within 15 iterations.

Supplementary Video 4. A 4×4 sample dynamically morphing six abstract shapes.

A 4×4 sample dynamically morphing six abstract shapes (Shape I–VI in Extended Data Fig. 5a) with the actuation voltages (designed via model-driven approach) updated at a rate of 10 fps. An in-situ 3D imaging provides a time-aligned 3D reconstruction of the morphing surface.

Supplementary Video 5. A 4×4 sample morphing into a target abstract shape against extrinsic mechanical disturbance via the experiment-driven process.

A 4×4 sample self-evolving into a target shape (Shape III in Fig. 3b) demonstrates an ability to self-adjust against mechanical disturbance. The first column shows the video recording of an undisturbed self-evolving process, time-synced with the 3D-reconstructed surface and the corresponding error map. The second column shows a situation where an external load (~0.1 g) is applied on a serpentine beam. In the third column, the sample continues to self-evolve to adapt to the additional loading.

Supplementary Video 6. A 4×4 sample demonstrating a semi-real-time morphing scheme via experiment-driven approach to learn the continuously evolving surface of a palm in-time.

The experiment-driven approach delivers a semi-real-time morphing scheme to learn the continuously evolving surface of a real object in-time. A duplicated stereo-imaging setup reconstructs the shapes of the palm surface using a 4×4 array of markers. The optimization acts directly to minimize the normalized displacement difference between the 16 markers and their corresponding nodes of a 4×4 sample. The hand movement is captured by Optical cameras captures the hand movement and the evolving sample. The videos are shown with a frame-to-frame alignment.

Supplementary Video 7. A 3×3 sample self-evolving toward multifunctionality.

A 3×3 sample with 9 reflective gold patches self-evolves via an experiment-driven process to perform an optical function and a structural function simultaneously. The optical function is to reflect and overlap two laser spots on a receiving screen. The structural function is to control the deformation of the central node of the sample to achieve the target displacement (-0.5 mm). The video combines and aligns the videos of the receiving screen, the evolving sample, and the ex-situ 3D reconstruction of the shape-shifting process, along with the loss functions over the number of function evaluations.

References

[S1] Mao, G. et al., Soft electromagnetic actuators. *Sci. Adv.* **6**, eabc0251 (2020).
[S2] Supplementary Note in: Zhang, F. et al., Rapidly deployable and morphable 3D mesostructures with applications in multi-modal biomedical devices. *Proc. Natl. Acad. Sci. U.S.A.* **118**, e2026414118 (2021).
[S3] Camacho, J. M. & Sosa, V. Alternative Method to Calculate the Magnetic Field of Permanent Magnets with Azimuthal Symmetry. *Rev. Mex. física E* **59**, 8–17 (2013).
[S4] Zhao, H.B. *et al*. Compliant 3D frameworks instrumented with strain sensors for characterization of millimeter-scale engineered muscle tissues, *Proc. Natl. Acad. Sci. U.S.A.* **118**, e2100077118 (2021).
[S5] Zhang, Z. A flexible new technique for camera calibration. *IEEE Trans. Pattern Anal. Mach. Intell.* **22**, 1330–1334, (2000).
[S6] Haralick, R. M. Solving camera parameters from the perspective projection of a parameterized curve. *Pattern Recognit.* **17**, 637–645 (1984).